Check for updates

Research progress on the epitaxial growth of hexagonal boron nitride on different substrates by the CVD method

Zikang Li, [ab] Zanbo Wang,[a] Quan Zhang,[a] Xiaoqi Bai,[a] Lingxiang Peng,[a] Chuntai Liu [b] and Zhiqiang Yao [*a]

Hexagonal boron nitride (h-BN) has a hexagonal structure similar to graphene, comprising alternating boron and nitrogen atoms. This unique structure endows h-BN with a plethora of excellent properties, including a low dielectric constant, elevated thermal and chemical stability, substantial mechanical rigidity, and an exceptionally low friction coefficient, rendering it versatile across a spectrum of applications ranging from semiconductors to aerospace. Moreover, its smooth surface, absence of dangling bonds, and wide band gap make h-BN an optimal substrate and gate dielectric material for two-dimensional electronic devices. This article details the synthesis methodologies and research progress of h-BN epitaxial growth on solid transition metal, liquid metal, alloy, sapphire/metal and semiconductor substrates. In particular, progress in improving the quality and functionality of h-BN films by adapting processes and substrates has been rigorously reviewed. Finally, the characteristics of different substrates are summarized and the challenges faced by h-BN in future applications are discussed.

1 Introduction

Since boron nitride was synthesized by Balmain from molten boric acid and potassium cyanide in 1842, it has been continuously studied by scientists, and even today, it is still considered to be one of the most promising inorganic materials of this century. With its impressive properties including high mechanical rigidity, elevated thermal and chemical stability, low dielectric constant (electrical insulation), and a very low coefficient of friction, boron nitride is widely used in the semiconductor industry and aerospace endeavors.[1–5] Beyond its traditional uses as lubricants, abrasive materials, optimal substrates for two-dimensional materials, and packaging components,[6] the recent revelations of boron nitride's distinct attributes in the fields of electronics and optics have helped to further expand its applications, making it a promising new generation emitter and detector in the DUV spectral range (Fig. 1).[7]

Four structural types of boron nitride have been reported, namely amorphous boron nitride (a-BN), hexagonal boron nitride (h-BN), cubic boron nitride (c-BN) and wurtzite boron nitride (w-BN).[8] Both h-BN and c-BN are stable forms of BN, so

the research on boron nitride mainly focuses on c-BN and h-BN.[9] Characterized by an sp^3 hybrid layered structure, c-BN assumes a cubic arrangement wherein each boron atom is intricately bonded to four nitrogen atoms. Due to its diamond-like configuration, c-BN is considered second only to diamond in hardness and thermal stability.[10] h-BN belongs to the sp^2 hybrid type, in which boron atoms and nitrogen atoms are connected by strong covalent bonds and alternately form a hexagonal network layer, yielding a hexagonal lattice reminiscent of a honeycomb structure similar to graphene. Owing to its structural and property similarities to graphene, the two-dimensional h-BN is also known as "white graphene".[11]

As we know, two-dimensional materials and their van der Waals heterostructures have received a lot of attention due to their unique properties and potential applications. As a typical two-dimensional material, graphene has high intrinsic mobility,[12] high Young's modulus and tensile strength,[13] high thermal conductivity[14] and good electrical conductivity.[15] The two-dimensional hexagonal boron nitride has a hexagonal structure similar to graphene, and the sp^2 bonds between the atoms in the layers are very strong,[16–20] while the van der Waals forces between the layers are very weak.[19–21] The similar structure leads to some similar properties of the two, and the strong covalent bond between the atoms makes hexagonal boron nitride also have excellent chemical stability, thermal stability and high mechanical strength.[11,22–24] In addition, both h-BN and graphene are anisotropic due to the weak van der Waals forces between the atomic layers, for example, the permittivity of h-BN in the out-of-plane direction is much smaller than that in the in-

aSchool of Materials Science and Engineering, State Centre for International Cooperation on Designer Low-Carbon and Environmental Materials, Zhengzhou University, Zhengzhou 450001, China

bKey Laboratory of Materials Processing and Mold Ministry of Education, National Engineering Research Center for Advanced Polymer Processing Technology, Zhengzhou University, Zhengzhou 450002, China
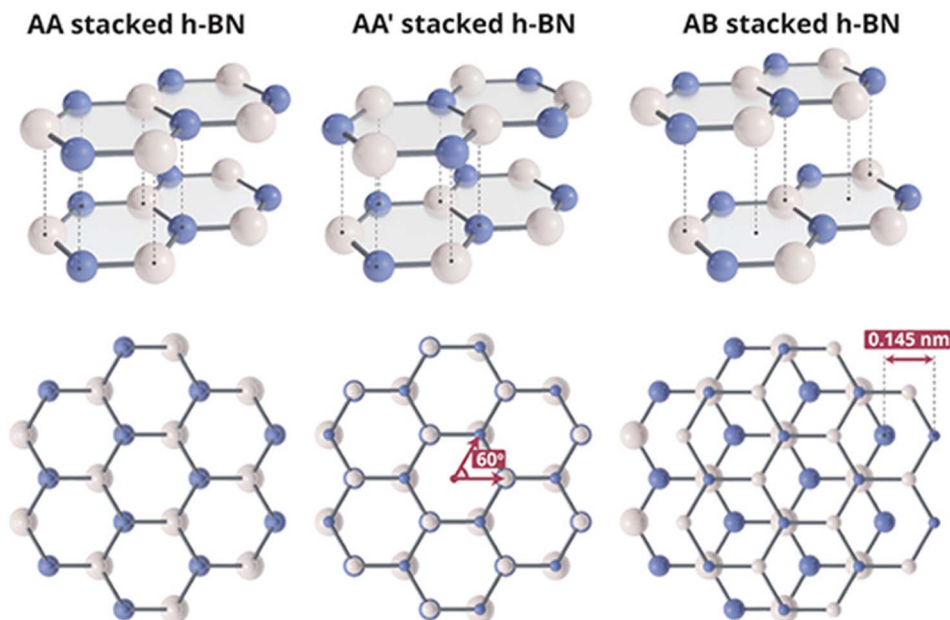
Fig. 1 Schematic diagram of the multi-type structure of h-BN.[7]

plane direction.[25] Although the atoms in the plane are covalent bonds, the electronegativity of the nitrogen atoms in h-BN is different from that of the boron atoms, and the electrons are closer to the nitrogen atom, breaking the symmetry of the electron configuration, which makes h-BN also anisotropic in the direction of the plane, while graphene remains isotropic in the plane. In addition, single-layer h-BN has a wide band gap (about 6 eV) and is an insulating material, while graphene is known to be a good conductor.[26] The optical band gap of h-BN shows a dependence on the number of layers, with a multilayer exhibiting an indirect band gap and a monolayer exhibiting a direct band gap.[27–29] This novel structural property gives h-BN excellent electrical and optical properties. High transmittance in the visible light region and a high absorption coefficient (about 10^5 cm^{-1}) in the deep ultraviolet (DUV) region make h-BN have broad application prospects in light detectors and light-emitting devices.[30,31]

Due to the weak van der Waals forces between layers, mechanical exfoliation is a reliable method to obtain single-layer graphene and h-BN.[32,33] As a top-down synthesis method, both mechanical exfoliation and chemical exfoliation can yield high-quality 2D h-BN flakes,[34] with the advantage of relatively low cost and simplicity. But the exfoliation technique also has disadvantages. On the one hand, using h-BN on a large scale is not feasible due to the small sample size usually obtained using the exfoliation process.[35,36] On the other hand, the experimental principles limit the precise control of the number of layers in h-BN. Chemical vapor deposition (CVD) belongs to the bottom-up approach and has the advantage of growing large-area, high-crystallinity h-BN. In recent years, there have been several examples of successfully synthesizing high-quality and single-crystal h-BN films using Cu and Ni transition metal substrates.[37,38]

At present, there is still a gap between the theoretical research of h-BN in the laboratory and its practical application in industrial production. In order to meet the requirements of h-BN in industrial applications, such as wafer-level size, controllable layer number, excellent crystalline quality, and single crystal growth, it is essential for thorough examination of the substrate type, surface condition, and interaction with h-BN. In this paper, the recent advances in the synthesis of two-dimensional h-BN by CVD are reviewed, and the effects of substrates on the growth of h-BN films are discussed. Finally, the characteristics of different substrates used for the growth of h-BN films are summarized, and the challenges faced by h-BN applications in the future are also discussed.

2 The mechanism of CVD growth of h-BN

The epitaxial growth of h-BN using CVD technology has a history of several decades, and in recent years, there has been significant progress in the application of this technology, particularly in the growth of high-quality single-crystal h-BN and control over the number of layers in h-BN thin film. To achieve controlled growth of h-BN, a clearer understanding of the mechanism behind CVD is necessary. Chemical vapor deposition is a process that involves the application of gaseous substances to induce chemical and transport reactions on a solid surface, resulting in the deposition of a solid material. The main steps include precursor molecules being heated to form volatile substances, the adsorption of these volatile substances on the substrate after evaporation, chemical reactions leading to nucleation, and the formation of a thin film.[39] Taking the precursor ammonia borane as an example, during the growth of h-BN, the ammonia borane precursor ($NH_3 \cdot BH_3$)
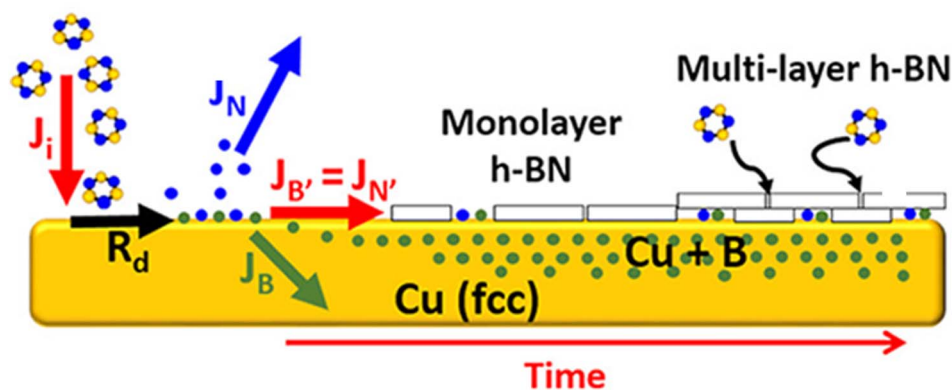
Fig. 2 Schematic diagram of the growth mechanism of h–BN on Cu, where J_i represents the impact flux of the precursor boron and nitrogen, R_d is the dissociation rate of the precursor, J_B is the diffusion flux of B towards Cu, and J_N is the diffusion flux of N leaving Cu. The formation of h–BN on Cu requires $J_{B'} = J_{N'}$.[41]

decomposes upon heating to produce borazine ($B_3N_3H_6$), monomeric aminoborane ($BH_2 \cdot NH_2$), and hydrogen gas as gas products, which then continue to participate in the reaction.[40]

Illustrated in Fig. 2 are the surface dynamics underlying the growth of 2D h–BN on copper. As the precursor molecule diffused onto the Cu substrate, it further dissociated into B and N atoms. The B atom has sufficient solubility in Cu at high temperatures, while the N atom is expelled from the surface due to its low solubility in Cu. The formation of h–BN on the substrate requires a balance between B and N elements, indicating that the formation of h–BN should be more complex than that of graphene.[41] It is worth noting that during cooling after growth, all the B atoms precipitate out of Cu, so the Cu catalyst remains in its metallic state throughout the entire CVD process, without the formation of borides or nitrides. However, in the case of Ni substrates, after growth and cooling, the B atom reacts with Ni to form borides of Ni.

3 The influence of substrates on the growth of h–BN

Substrates play a key role in the growth of h–BN, with the growth density of domains, the orientation of domains, the roughness of films, and the control of layers all closely related to the type and form of the substrate. Therefore, exploration and discussion of substrates play an important role in the study of h–BN growth behavior. For example, a substrate with a rough surface will have a relatively lower surface energy, resulting in a h–BN film with a higher nucleation density and grain boundary density. The smooth surface substrate will make the as-prepared h–BN have a relatively smaller grain boundary density and larger domains. The liquid metal surface provides a dynamic platform, which enables h–BN domains to have a certain ability of rotation and movement, and has the opportunity to realize the self-alignment of the domains.

3.1 Solid transition metal substrates

This section is mainly used to introduce the research progress on the growth of h–BN on the most common solid transition

metal foil substrates. As early as 1990, Paffett synthesized the first h–BN monolayer by decomposing $B_3N_3H_6$ on transition metals such as Pt(111) and Ru(0001) using Chemical Vapor Deposition (CVD) in an Ultra-High Vacuum (UHV) system.[42] However, ultra-high vacuum systems are highly complex and have certain limitations, such as the difficulty of transferring h–BN from the growth substrate to other substrates. Therefore, nowadays, most researchers use atmospheric pressure CVD (APCVD) and low-pressure CVD (LPCVD) techniques with transition metals as catalytic substrates for large-scale and controllable growth of 2D h–BN, such as Cu(111),[38,43] Cu(110),[44] Ni(111),[40,45] Pt(111),[31] Fe,[46] Au,[47] Pd(111),[48,49] and Rh(111).[44]

Song et al. used a 25 μm thick polycrystalline copper foil substrate, which was quickly rinsed with diluted nitric acid and deionized water. h–BN films consisting of 2–5 atomic layers were successfully synthesized in the LPCVD system using ammonia borane as a precursor and Ar/H_2 as a carrier gas.[50] However, they were unable to obtain a monolayer of h–BN. The researchers suggested that growth occurs through surface-to-mediated processes, so the quality of the copper foil plays a key role in controlling the formation of continuous layers on the substrate and the number of h–BN layers formed. In contrast, Kim et al. utilized the advantages of LPCVD, where the growth is predominantly steered by surface reactions and less affected by the substrate geometry or gas flow effects, to achieve a monolayer h–BN thin film.[51] Their investigations revealed that the nucleation sites of h–BN are influenced by the growth substrate surface morphology, as there may be more impurity sites on the copper surface along the rolling direction, fostering the concentration of nucleation domains. Furthermore, electrochemical polishing of the copper surface culminates in a remarkably smooth and flat surface, which results in a more uniform distribution of nucleation sites on the copper surface and an increase in the average size of the triangular islands.

In general, larger grains will also produce lower grain boundary densities per area in the film, resulting in higher film quality for electronic device applications. Diminishing nucleation density facilitates the growth of individual h–BN grains to larger dimensions, a phenomenon substantiated by numerous

investigations. Tay *et al.* used phosphoric acid as an electrolyte in the electrochemical polishing of copper foil. Polished copper with a smooth surface has smaller roughness, and higher effective surface energy is expected to increase the Gibbs free energy barrier, thus limiting nucleation,[45] which leads to a significant increase in the size of single h-BN domains after growing up, with the largest domain size up to 35 μm^2. A smoother continuous h-BN film with fewer grain boundary defects can therefore be created when the domains merge. In addition, it can be observed that the h-BN domains grown *via* this method are hexagonal, which is due to the oxidation of the surface by the reaction of Cu with the phosphoric acid (H_3PO_4) electrolyte during electropolishing. The oxidation of copper reduces the edge adhesion energy barrier, and BN free radicals have enough energy to bond to both N and B ends. This leads to the formation of hexagonal h-BN domains.

In addition to triangular and hexagonal h-BN domains, circular, trapezoidal, rectangular, truncated triangular, and truncated hexagonal domains are all possible single-layer h-BN domains.[52] Ji *et al.* found that in addition to triangles and hexagons, other crystal domains with different shapes would

appear on different copper grains on the same copper foil, which researchers attributed to the influence of Cu grain orientation, as shown in Fig. 3(a).[53] With the gradual in-depth study, Stehle *et al.* found that the transformation of the h-BN shape from triangle to hexagon was affected by the ratio of N to B active components on the Cu surface, as shown in Fig. 3(b).[54] Researchers changed the ratio of N and B radicals by adjusting the distance between the Cu substrate and the precursor, increasing the growth temperature, and changing the buffer gas from argon to nitrogen. Finally, it is concluded that h-BN crystals are N-terminal triangles under N-rich conditions, while h-BN crystals can evolve into truncated triangles or hexagons under B-rich conditions.[46,56–59] Other complex shapes are derived from the concatenation of several single crystal h-BN domains, as shown in Fig. 3(c) and (d).[55]

Since nucleation predominantly occurs in high surface energy regions such as grain boundaries or impurity locations, in addition to surface polishing of the substrate, the nucleation density can be adjusted by improving the surface crystallinity of the substrate. Wang *et al.* reported the favorable influence of copper foil in diminishing nucleation density and fostering the
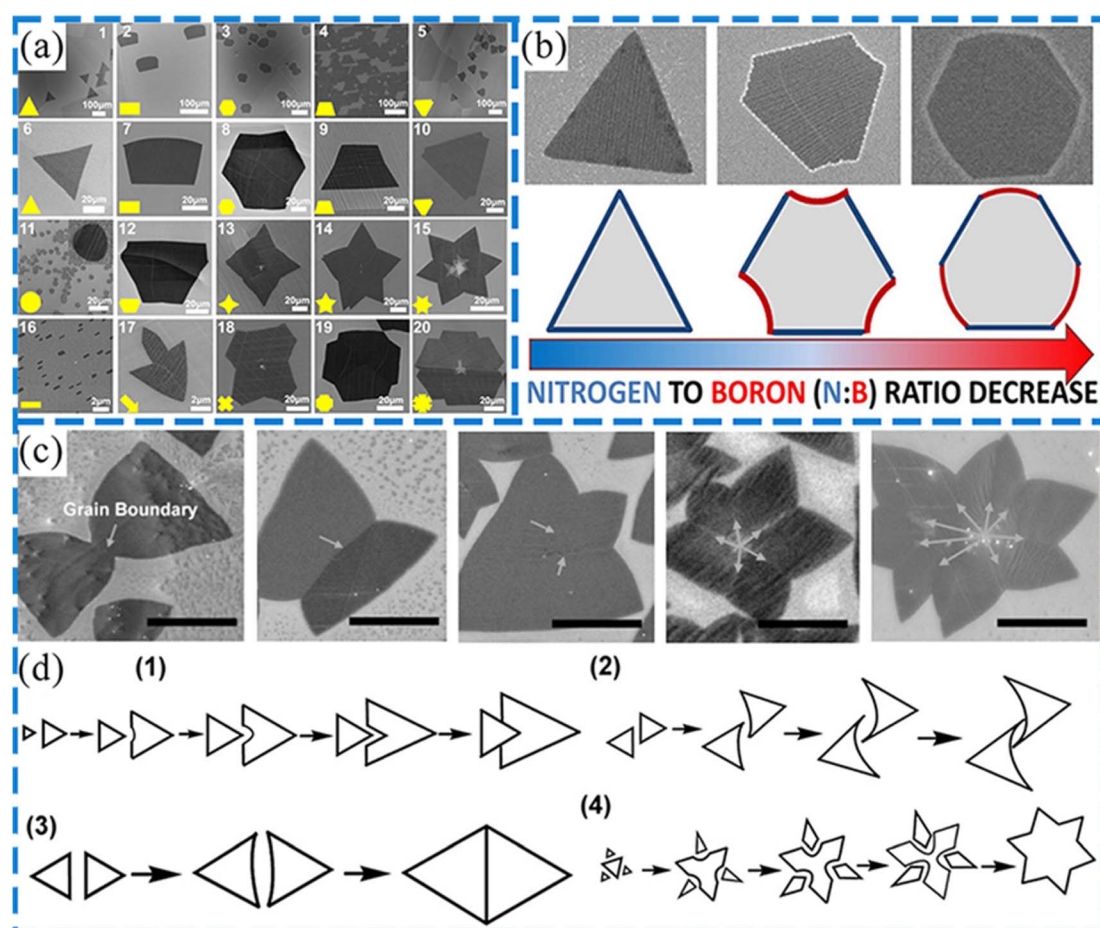

Fig. 3 (a) Varied h–BN domain shapes;[53] (b) SEM images of h–BN crystals with different shapes along with a sketch of the resulting h–BN crystal shapes and corresponding B and N terminations;[54] (c) typical SEM images of h–BN flakes with various complex structures. Note that grain boundary lines can be seen and labeled by arrows;[55] (d) the models for the dynamic merging process of h–BN flakes, where (1–3) represent cases for point-to-edge, partly and fully edge-to-edge merging. The model (4) describes a process for constructing a perfect star-like structure using triangular building blocks.[55]

expansion of sizable h-BN grains after annealing at 1050 °C.[60] High temperature annealing can effectively eliminate grain boundaries or defects on the substrate, resulting in an increase in the grain size and an improvement in surface smoothness. As shown in Fig. 4(a)–(c), when the annealing time is 0, 3 and 6 h, the size distribution of h-BN slices varies from 1–5 μm to 3–10 μm to 5–20 μm, respectively. With the increase of annealing time, the size of h-BN also increases. Ji et al. combined a poly-crystalline Cu shell made of thick copper foil (127 μm), high pressure pre-annealing and zigzag curved copper foil inserted into the shell, and successfully obtained single-crystal h-BN domains with a transverse size of up to ∼300 μm and continuous h-BN films with an average grain size of ∼100 μm (Fig. 4(d)–(f)).[53] The thick Cu shell inhibits the diffusion of boron and nitrogen radicals to the interior. Pre-annealing the substrate under high pressure helps to ameliorate pronounced wrinkles, steps, and imperfections, thereby enhancing the Cu substrate's integrity. The zigzag bent shape of the copper foil inserted into the copper bag increases the surface area of the copper. These three strategies synergistically collaborate to diminish the nucleation density and increase the grain size of h-BN.

It is not difficult to find that, although reducing the nucleation density effectively improves the grain size of h-BN and reduces the grain boundary density, obtaining a large area of continuous single crystal h-BN film is difficult by simply lowering the nucleation density. Therefore, the researchers turned their attention to the method of directly obtaining single or less oriented h-BN triangular crystal domains and combining them into large single crystals. Song et al. found that the orientation of h-BN monolayers is closely related to the crystal orientation of the Cu substrate.[61] The orientation of h-BN triangular domains grown on polycrystalline copper foil is irregular, while the orientation of h-BN domains grown on

Cu(111) has two main orientations (orientation deviation is 60°). On the Cu(100) and Cu(110) planes, there are 4 and 6 orientations respectively, as shown in Fig. 5(a)–(f). Furthermore, the rotation of the h-BN lattice on the entire film is less than 1.06° because of the slight lattice mismatch between the Cu(111) plane (2.556 Å) and h-BN (2.500 Å), suggesting that the arrangement of the h-BN film and the Cu(111) crystal plane is satisfactory. Hite et al. also pointed out that the growth rate of h-BN is inversely proportional to the surface energy of Cu, and h-BN grows fastest (has maximum effective thickness) on the surface of Cu(111) and slowest on the surface of Cu(110), as shown in Fig. 5(g)–(j).[62] If you are concerned about the growth rate of h-BN, the Cu(111) substrate may better match your expectations.

Obtaining large area single crystal metal substrates, such as Cu(111), is crucial for growing large area aligned h-BN grains.[47] Brown et al. produced long-range crystallinity in Cu foil by annealing it for up to 12 hours at a temperature of 1030 °C, which is close to its melting point, in an Ar/H$_2$ environment.[63] This process produces a single Cu(111) domain with an area of up to 16 cm^2 with spatially uniform in-plane orientation over the entire foil. The resulting h-BN films display uniform crystalline alignment. In addition to direct annealing at the melting point of the substrate, a highly uniform Cu surface can also be obtained by growing the substrate by melting. Tay et al. melted and resolidified polycrystalline copper foil on W foil to prepare single crystal Cu(110).[64] The orientations of the h-BN domains are predominantly consistent with ∼75% grain alignment of up to millimeter-range. It is worth noting that the surface quality of molten resolidified copper foil has a great relationship with the cooling rate during solidification. When the re-solidification rates are less than or equal to 1 °C min^{-1}, the non-uniform lines on the surface are reduced to the minimum. Jin et al. used quartz holders for 'holding' (hanging) the Cu foil, holding
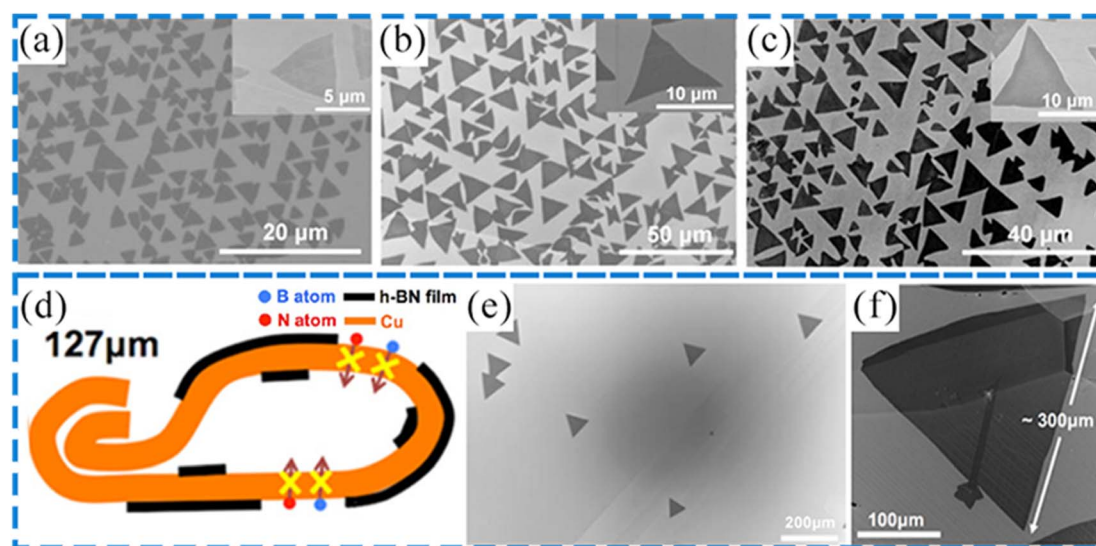

Fig. 4 (a) SEM images of triangular h-BN domains grown on Cu foil without pre-annealing;[60] (b and c) SEM images of h-BN domains after annealing the Cu surface for 3 h and 6 h, respectively;[60] (d) schematic diagram of the growth mechanism of h-BN on 127 μm copper foil;[53] (e) SEM image of h-BN grown without high pressure pre-annealing;[53] (f) SEM image of large-sized h-BN triangular domains grown on 127 μm copper foil.[53]
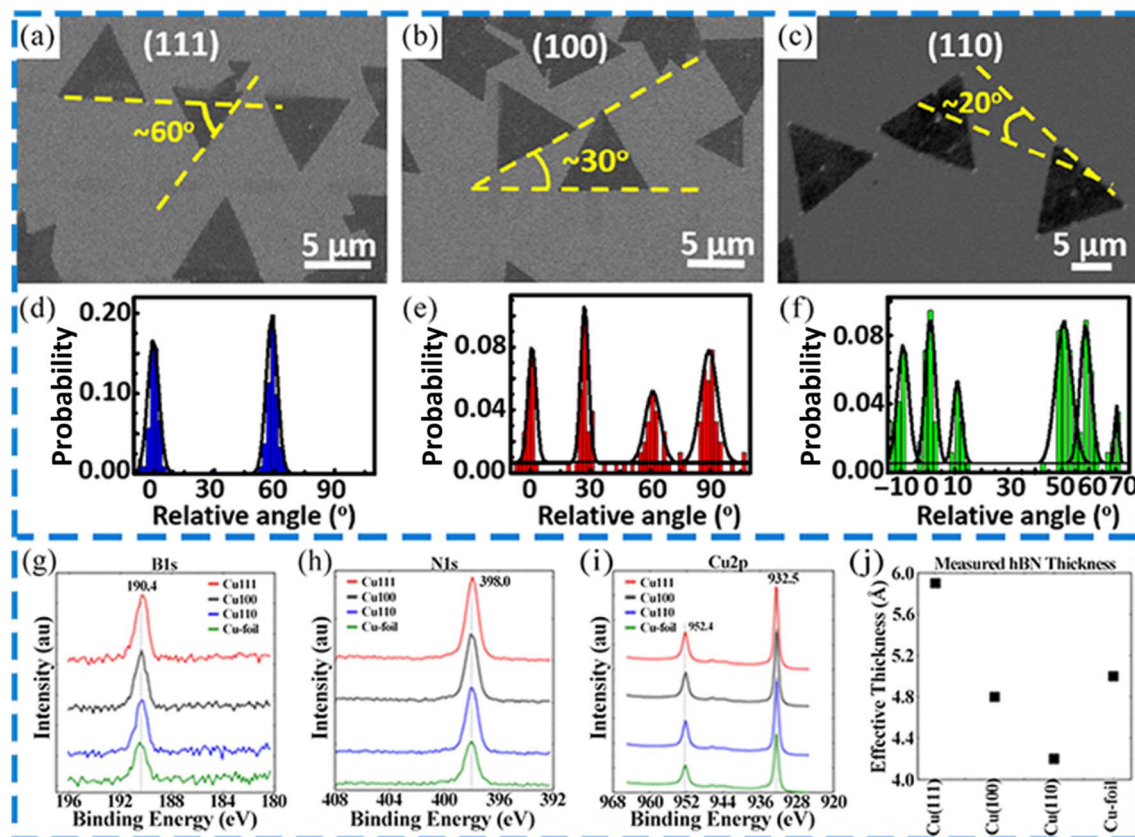
Fig. 5 (a–c) Representative SEM images of h-BN grown on Cu(111), Cu(100), and Cu(110) surfaces;[61] (d–f) statistical distributions of the edge angles of individual triangular h-BN domains grown on Cu(111), Cu(100) and Cu(110) faces, respectively;[61] (g–j) XPS spectra of h-BN on Cu(111), Cu(100), Cu(110) and Cu foil. The binding energies correspond to (g) B 1s, (h) N 1s, and (i) Cu 2p, and (j) the calculated thickness of the h-BN film.[62]

it at 1050 °C and in a H₂/Ar flow atmosphere for 12 hours, to prepare 32 cm² bulk single crystal Cu(111).[65] In the same work, this method, known as contactless annealing, can also be used to obtain large sizes of Ni(111), Co(0001), Pt(111) and Pd(111) single crystal foil substrates.

In fact, the closely packed Cu(111) crystal faces have the lowest surface energy of all the crystal faces, so since the surface energy is minimized, they should spontaneously transform into grains with Cu(111) surfaces. The previously mentioned transformation could be hampered by other energy terms, such as the strain energy brought by thermal stress, which might be higher than the surface energy. For example, the non-contact annealing mentioned above eliminates or at least minimizes the deformation of thermal stress due to interface contact by suspending the metal foil, and its principle is shown in Fig. 6(a).[65] In addition, the proportion of a certain orientation in polycrystalline copper foil can be artificially increased by various strategies to form a "seed layer", and a large area single crystal substrate with a single orientation can be formed according to the principle of minimum surface energy. According to this principle, the seed layer can accelerate the transverse diffusion of Cu grain boundaries along the copper foil, rather than just horizontal diffusion.[66] As shown in Fig. 6(b)–(d), Wang et al. placed a small piece of monocrystalline Cu(110) on polycrystalline copper foil and then annealed it at high temperature to obtain a 100 cm² Cu(110) substrate.[67] In

addition, Wu et al. also formed a variety of large single-crystal copper foil substrates with high refractive index surfaces, such as (113) and (123), on the surface through mild pre-oxidation of polycrystalline copper foil, the principle of which is shown in Fig. 6(e).[68] However, the appearance of some high index seeds is a random event, so the researchers cut a small piece of high index single crystal copper from the large single crystal copper foil obtained by annealing and placed it on the polycrystalline copper foil as the "seed layer", thus achieving a stable way to obtain the high index surface. Using this method, three high refractive index single crystal nickel foil substrates (012), (013) and (355) were also prepared. Chen et al. found that a CuₓO(111) nanocrystalline structure could be formed on the surface of copper foil after 30 min pre-oxidation at 400–450 °C.[66] Then, the CuₓO nanocrystal-dominated structure is transformed into a Cu(111) seed layer on the Cu surface by further reduction of copper oxide, which promotes the rapid formation of large area single crystal Cu(111).

The epitaxial growth of unidirectional domains is related to the symmetry of h-BN and the symmetry of the substrate, while h-BN has a lower symmetry (C₃ᵥ) and is incompatible with substrates with higher symmetry.[69–71] Consequently, on the Cu(111) surface, two orientations of h-BN crystal domains are typically obtained, making it challenging to obtain single-crystalline h-BN. This is in accordance with the related research content mentioned in the earlier part of this article.
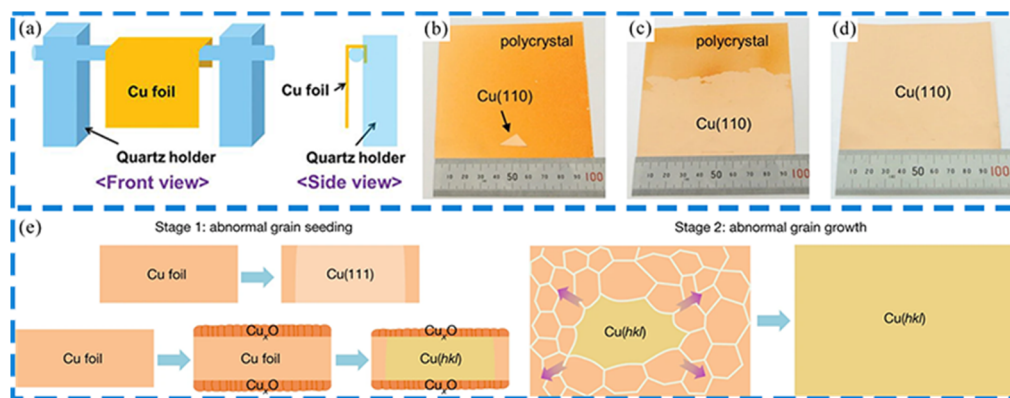
Fig. 6 (a) Schematic diagram of the device for preparing single crystal Cu(111) foil by contactless annealing. A small piece of single-crystal Cu(110) with ⟨211⟩ steps was placed on polycrystalline Cu foil of size 10×10 cm^2 to guide the annealing of the Cu foil;[66] (b) after annealing at 1040 °C for 5 min, the nucleus has started to assimilate the polycrystalline Cu foil;[67] (c) after annealing for 2 h, about three-fifths of the Cu foil was annealed to give single-crystal Cu foil;[67] (d) after annealing for 5 h, the entire foil is single-crystal Cu foil;[67] (e) schematic diagram of pre-oxidation-induced seed growth of high-index single crystal copper foil. Stage 1: without an oxide layer, Cu(111) has the lowest surface energy and is the main growth surface. Once the oxide layer forms, high-index Cu(hkl) will grow, forming abnormal grain seeds. Stage 2: large abnormal grain seeds consume small normal grains around them, eliminating the grain boundaries of the copper foil.[68]

Nevertheless, if one desires to obtain single-oriented h-BN single-crystalline films, one can refer to the relevant research by Chen *et al.* They employed the sputtering method to fabricate Cu(111) single-crystalline films on sapphire surfaces, reducing the symmetry under the influence of sapphire steps. Subsequently, high-quality single-crystalline h-BN films were prepared on the Cu(111) surface *via* the LPCVD method, as shown in Fig. 7(a)–(d).[72] Another method is to prepare h-BN directly on the substrate surface with lower symmetry. Wang *et al.* reported the epitaxial growth of 100 cm^2 single crystal h-BN monolayers obtained by annealing industrial copper foil on adjacent surfaces with low symmetry Cu(110), as shown in Fig. 7(e)–(g).[73] The principle of this method is that the coupling of Cu ⟨211⟩ step edges and h-BN zigzag edges achieves epitaxial growth, which breaks the equivalence of anti-parallel h-BN

domains and makes the unidirectional domain orientation approximate to more than 99%. The researchers further investigated the mechanism of the step growth of single crystal h-BN: (1) a certain degree of bending on the microscopic scale of the substrate step does not affect the single orientation of h-BN, if their kinks have similar dimensions with negligible mismatches, $\delta_K < 0.1$ Å. (2) Stronger chemical affinity of metal to the N atoms at the zigzag edge of h-BN singles out its particular orientation, without evidence of any epitaxy, at the edge or to the surface. (3) Molecular dynamics simulation shows that the step height of the substrate should be smaller than that of the BN bond in order to achieve seamless splicing across the step, that is, $s < 1.44$ Å.[74]

Transition metal Ni is one of the common substrates for growing h-BN. Ni(111) has an in-plane interatomic distance of
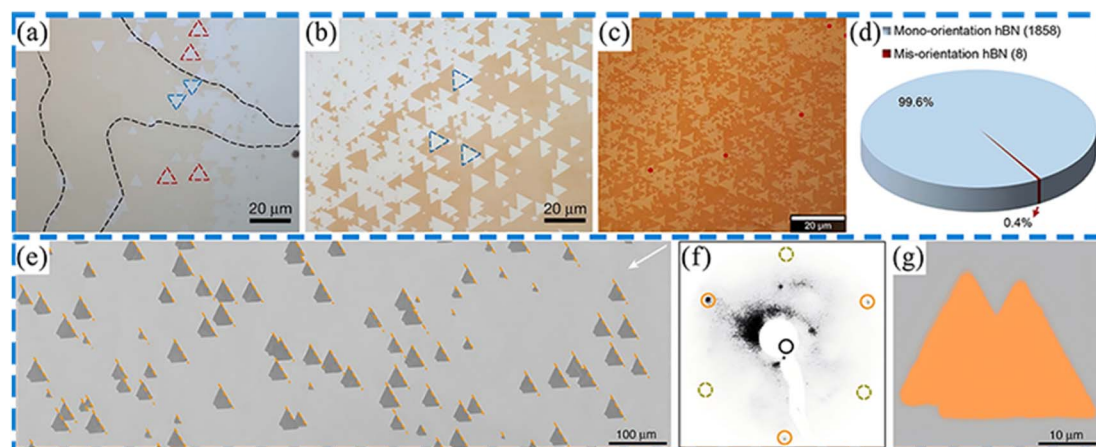

Fig. 7 (a) Optical microscope image of h-BN grown on different Cu(111) grains. Black dashed lines indicate twin grain boundaries;[72] (b) mono-oriented h-BN flakes on single-crystal Cu(111) films;[72] (c) optical micrograph of h-BN grown on a Cu(111)/c-sapphire substrate at 1050 °C. Misaligned h-BN flakes are marked by red circles;[72] (d) statistical analysis of the optical micrograph from (c), more than 99.6% of the h-BN flakes are aligned in one direction on Cu(111);[72] (e) SEM image of unidirectionally aligned h-BN domains grown on Cu(110);[73] (f) LEED pattern of as-grown h-BN;[73] (g) polarized SHG mapping of two unidirectionally aligned h-BN domains.[73]

2.49 Å, which is very close to the h-BN lattice constant of 2.50 Å. So, there is a small mismatch (about 0.4%) between the nickel substrate and h-BN.[75] As early as 1995, scholars exposed borazine to Ni(111) at high temperatures (>700 °C) to obtain ordered h-BN monolayers, but this method required expensive ultra-high vacuum (UHV) chambers. Moreover, under ultra-high pressure conditions, the growth of h-BN seems to be limited to monolayers, making multilayer growth difficult. Hence, Oh et al. adopted a chemically–mechanically polished (CMP) single crystal Ni(111) substrate, and used the APCVD technique to create a centimeter-sized single crystal h-BN film heteroepitaxy on the Ni substrate, and successfully separated the h-BN film from the substrate by the electrochemical stripping method, allowing the Ni(111) substrate to be used repeatedly for the next round of growth, as shown in Fig. 8(a)–(c).[76] Cho et al. pretreated nickel foil by electrochemical polishing (ECP) and annealed in hydrogen at atmospheric pressure, then grew h-BN on Ni foil by the CVD method, and studied its growth kinetics.[77] They pointed out that the rate-determining step will be the dissociative chemisorption of radicals and molecules containing boron, nitrogen and hydrogen. The adsorption rate (R_{ads}) is proportional to the sticking coefficient (S) and flux (Hertz–Knudsen). Because the flux was fixed in their experiments, the sticking coefficient was

the key to elucidating the rate difference. The sticking coefficient is predominantly governed by the surface energy. Vitos et al. reported that the surface energy depends on the crystalline orientation of Ni, and the surface energy of the Ni grains decreases in the order (110), (100), and (111).[79] This order reflects the contrast in the growth rate of h-BN. By comparing the area of the h-BN region grown on the grains with different orientations on Ni foil in Fig. 8(d), it can be seen that the growth rate of h-BN showed a contrast among 3 grains with different orientations. So, the growth rate of h-BN in Ni(110) and Ni (100) is higher than that of Ni(111). Ma et al. also successfully synthesized epitaxially grown wafer-level single crystal triple-layer h-BN on Ni(111) with steps obtained by non-contact annealing.[78] The researchers also found that due to the large solubility of B in nickel, boron would dissolve in Ni during the cooling process, forming a $Ni_{23}B_6$ interlayer between the monocrystalline h-BN film and the Ni matrix. By cross-sectional TEM measurements, they found the epitaxial relationship between $Ni_{23}B_6$ and Ni substrate with $[111]Ni_{23}B_6\|[111]Ni$ and $[002]Ni_{23}B_6\|[002]Ni$, as shown in Fig. 8(e)–(j).

Although the lattice mismatch between Pt and h-BN is large (7–10%), the interface interaction is weak, which may lead to the emergence of some interesting moiré structures.[80,81] As early as 1990, M. T. et al. found that there is an interesting
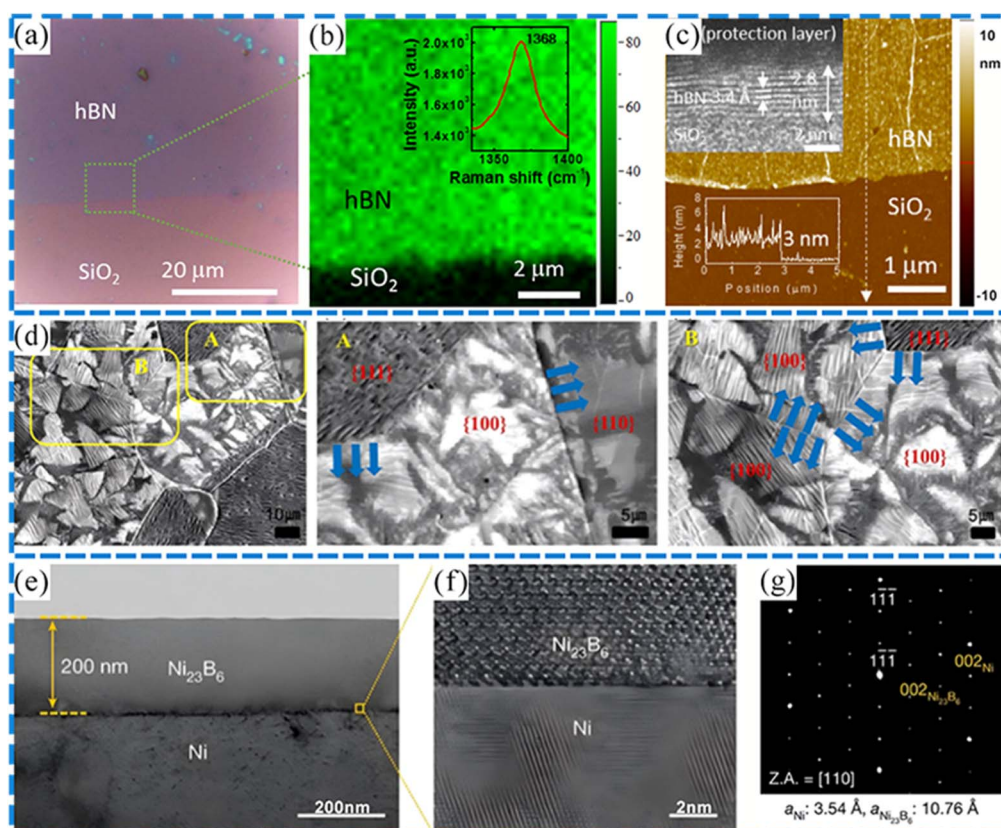

Fig. 8 (a) Optical microscope image of the h-BN film transferred onto a SiO$_2$/Si substrate;[76] (b) Raman map of the h-BN E$_{2g}$ peak;[76] (c) surface morphology of the h-BN film investigated by AFM;[76] (d) SEM image of h-BN grown on Ni foil (left); SEM image of area A (middle) and SEM image of area B (right), with the orientation of the grains on Ni foil marked in red;[77] (e) low-magnification TEM image of h-BN/Ni$_{23}$B$_6$/Ni grown for 60 min; the scale bar denotes 200 nm;[78] (f) high-magnification TEM image of the Ni$_{23}$B$_6$/Ni interface; the scale bar denotes 2 nm;[78] (g) SAED pattern of Ni$_{23}$B$_6$ and Ni.[78]

phenomenon between h-BN and Pt(111). The h-BN layer exhibits a specific symmetry on the Pt surface, and hexagonal point splitting is observed by low energy electron diffraction (LEED). This phenomenon indicates that there is a superstructure matching relationship between the h-BN layer and the surface lattice of Pt.[82] Kim et al. used the LPCVD method to synthesize high-quality monolayer h-BN on large-area Pt foil.[83] The temperature inside the LPCVD system was set to 1100 °C, and the precursor ammonia borane was heated to 130 °C. Maintaining invariant growth parameters, a uniform monolayer h-BN could be grown on the Pt foil regardless of how long the growth process lasted, without the formation of multiple layers. The electrochemical bubbling method is used as an alternative, allowing for the repeated use of the substrate after transferring h-BN, thus avoiding the wastage of Pt foil.

According to theoretical research, h-BN defects affect performance. However, if these defects are properly managed, new applications for the material's electrical and magnetic properties can be created.[84] In order to solve such issues, Qi et al. used Re(0001) as a substrate and h-BN was grown by the CVD method under UHV conditions.[85] Subsequently, h-BN was characterized by STM, and high quality h-BN crystal domains and a periodic (fixed period 3 nm) "nanonetwork" superstructure of (12 × 12) B–N/(11 × 11) Re(0001) were obtained on Re(0001), as shown in Fig. 9(a)–(f). According to the STM observations, three defect types were introduced at the patching interface: "heart-shaped" moiré defects and nonbonded and bonded line defects, as shown in Fig. 10. The "heart-shaped" defects significantly regulate the band position and band gap width (about 3.5–3.7 eV). Due to the existence of strong edge states, nonbonded line defects also reduce the band gap (about 3.5–3.1 eV). The bonded line defects reduce the band gap (about 3.7–3.3 eV).

The formation of defects in h-BN is not limited to boron/nitrogen vacancies,[89] but multiple defects can occur, such as carbon,[90] oxygen, and hydrogen impurities, and donor–acceptor pairs.[91] Innocenzi et al. reported the relationship between defects and photoluminescence (PL) in two-dimensional (2D) and zero-dimensional (0D) h-BN nanostructures. It is found that h-BN nanosheets exhibit fluorescence properties due to the presence of alternative oxygen atoms in their structure.[92]
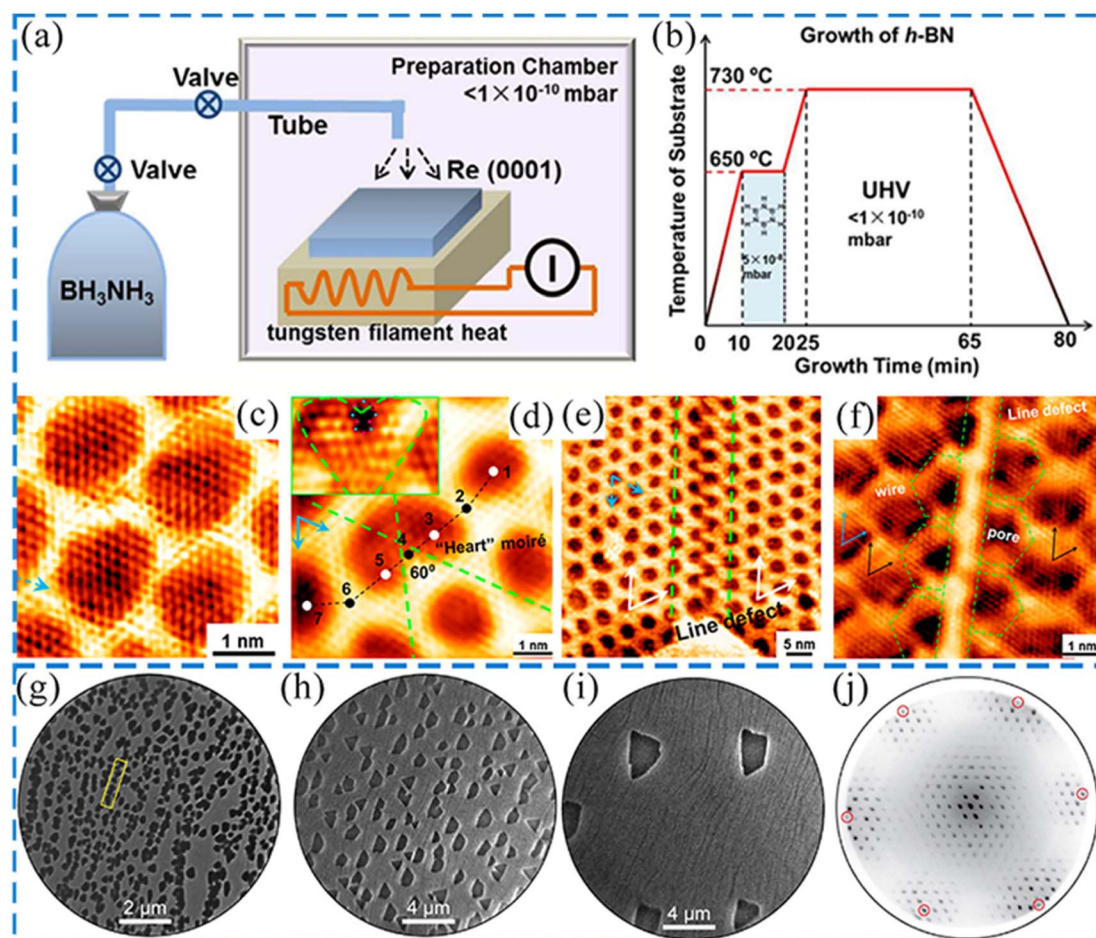

Fig. 9 (a) Schematic diagram of the ultrahigh vacuum chemical vapor deposition system;[85] (b) annealing process for h-BN growth;[85] (c–f) STM images of h-BN on Re(0001) ((d), (e) and (f) show the heart shape defect, nonbonded linear defect and bond linear defect respectively);[85] (g–i) LEEM images of h-BN islands synthesized at 800, 900 and 1100 °C after 100 s of borazine dosing at (g) 5×10^{-8}, (h) 5×10^{-8} and (i) 3×10^{-8} mbar, respectively;[86] (j) characteristic LEED pattern originating from several coalescing h-BN islands synthesized at 900 °C. Red circles indicate positions of first-order h-BN spots.[86]
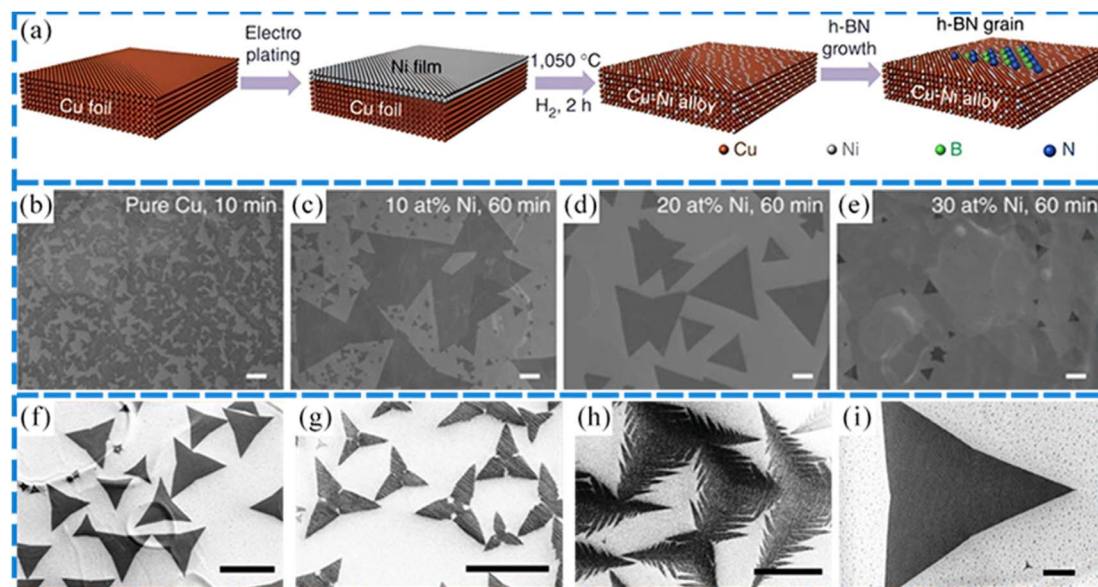
Fig. 10 (a) Schematic diagram of the growth process of h-BN on the Cu–Ni substrate;[87] (b) SEM image of h-BN grains grown on Cu foil for 10 min at 1050 °C;[87] (c–e) SEM images of h-BN grains grown on Cu–Ni alloy foil with (c) 10 atom%, (d) 20 atom%, and (e) 30 atom% Ni for 60 min at 1050 °C;[87] (f–h) scanning electron microscope (SEM) images showing the domain morphologies grown at (f) 1030 °C, (g) 1025 °C, and (h) 1015 °C, respectively. Scale bars are 100 μm in panel (f) and 20 μm in panels (g–h);[88] (i) SEM images showing the domains grown on the Cu substrate doped with ≈2.8 at% Si. Scale bars are 20 μm.[88]

Ru(0001) and Rh(111) have a strong interaction with h-BN, while Pt(111) and Cu(111) have a weaker interaction with h-BN.[93–95] For Ir(111), its interaction with h-BN is characterized as intermediate. This gives it a special quality: h-BN is bound to the substrate with a certain strength connection to allow for uniform orientation domain formation, but the bond is not too strong to maintain its inherent characteristics.[96,97] M. *et al.* successfully achieved the growth of high-quality h-BN monolayer islands by exposing an Ir(111) substrate to borazine by the CVD method in an UHV device. During growth, two forms of h-BN islands are observed: triangular and trapezoidal, which rotate 180° with respect to each other, as shown in Fig. 9(g)–(j). The growth of these islands is influenced by the Ir(111) surface step, which is the main location for island formation. The study of h-BN islands by LEEM shows that the combination of Ir(111) and triangular islands is stronger and the work function is higher. Trapezoidal islands have a lower work function, which indicates that they are weakly bound to Ir(111). In addition, triangular islands generally have higher electron reflectance, while trapezoidal islands exhibit lower reflectance. The difference between the two island forms can be attributed to the different ways in which they bind to the Ir(111) surface and the strength of their interaction. These differences not only affect the shape and growth patterns of h-BN islands but may also play an important role in future 2D material synthesis.[86]

3.2 Alloy substrates

The growth mechanism of h-BN on Cu is mainly surface-mediated, while the growth mechanism of h-BN on Ni is neither surface-limited nor dominated by segregation and precipitation of B and N. Instead, it depends on the surface chemistry of Ni–B and Ni–N.[98] Lu *et al.* found that the introduction of Ni on the Cu substrate can significantly reduce the nucleation density, as shown in Fig. 10(a)–(e).[87] Ten to twenty atom% of Ni can reduce the nucleation density to 60 per mm^2 and obtain h-BN grains with an area of ∼7500 μm^2. The nucleation density dropped further on 30 atom% Ni substrates, but the lateral growth rate dropped to ∼0.3 mm min^{-1}, with the largest grain side length only reaching ∼30 mm. Furthermore, when the Ni content was increased to 50%, no h-BN grains were observed even after 90 minutes of growth. The effect of nickel on the formation of large size h-BN particles was further explained using the density functional theory (DFT) calculation. The results show that increasing the Ni content in our alloy substrates in a certain range has two effects: on the one hand, the dehydrogenation of the precursor becomes easier; on the other hand, the decomposition energy of dehydrogenated derivative BN of the precursor decreases significantly. With the further increase of Ni content, the original surface-mediated growth mechanism based on the Cu substrate began to change to a new growth mechanism based on Ni–B and Ni–N solid–gas reactions, so that the growth of h-BN would be completely transferred to a different process window, resulting in a decline in growth rate and even no phase formation. In addition, graphene/h-BN heterojunctions were fabricated to evaluate the growth quality of h-BN. Based on the resistivity curves of typical graphene/h-BN and graphene/SiO$_2$/Si back-gate field-effect transistors, the calculated mobility is 6213 and 3625 cm^2 V^{-1} s^{-1}, respectively. This indicates that h-BN grown by CVD has better growth quality. Meanwhile. Lu *et al.* also successfully synthesized high quality graphene and hexagonal boron nitride monolayer in-plane heterostructures on the Cu–Ni alloy substrate. The Cu–Ni alloy substrate accelerates the

growth of graphene and greatly reduces the damage to the h-BN lattice.[99]

Although Cu–Ni alloys can reduce the nucleation density of h-BN, the corresponding maximum grain size is still limited to ≈ 100 μm. Li et al. introduced a small amount of silicon into the Cu substrate to achieve reliable control of the morphology and nucleation density of deposited h-BN domains.[88] The presence of silicon alters the growth mechanism from attachment-limited mode to diffusion-limited mode, producing a rich morphology and large domain size. When the doping concentration of Si is ≈ 2.8 atom%, the morphology of h-BN domains is fractal dendrites and shrunken shape at lower growth temperature. When the growth temperature increases close to the melting point, triangles dominate and their nucleation density decreases sharply by two orders of magnitude, resulting in large domains with a maximum transverse size of about 0.25 mm, as shown in Fig. 10(f)–(i). In fact, the sharp decline in the nucleation density of h-BN is not entirely dependent on the increase of silicon concentration in the substrate, but is closely related to temperature. The higher the Si content, the lower the melting point of the Cu substrate. When the Si content reaches ≈ 2.8 atom%, the alloy substrate begins to transition to the liquid phase and large domains appear at the deposition temperature of 1030 °C, which means that the phase transition from solid to liquid on the substrate surface can significantly inhibit the nucleation density.

Due to the relatively high solubility of B and N atoms in Fe metal, B and N atoms dissolved in the Fe metal can undergo a segregation process to form multi-layered h-BN.[100] Kim et al. grew large area h-BN films by the CVD method on a pre-annealed smooth Fe substrate surface, as shown in Fig. 11(a).[101] The thickness of h-BN (5–15 nm) was controlled by the cooling rate, that is, separated boron and nitrogen atoms precipitated in the Fe substrate at high temperatures. The 15 nm thick h-BN was characterized by XRD and AFM, and the test results are in agreement with the theoretical values. This reaction shows that the prepared films have better crystal quality. In addition, graphene, MoS_2 and WSe_2 devices were fabricated on top of h-BN with CVD growth,[103] as shown in Fig. 11(b)–(e).[101] The field-effect hole and electron mobility (μ_p and μ_n) and intrinsic doping level were extracted from the graphene FETs,[104] and the extracted hole mobility (μ_p) and intrinsic doping level (n_{dirac}) of the two substrates (h-BN and SiO_2) are shown in Fig. 11(c).[101] The average intrinsic doping level of monocrystalline graphene on h-BN is lower than that of the reference SiO_2 sample, which may be due to the low number of suspended bonds on h-BN. The carrier mobility of the device on the h-BN substrate exceeds 10 000 cm^2 V^{-1} s^{-1} with a peak
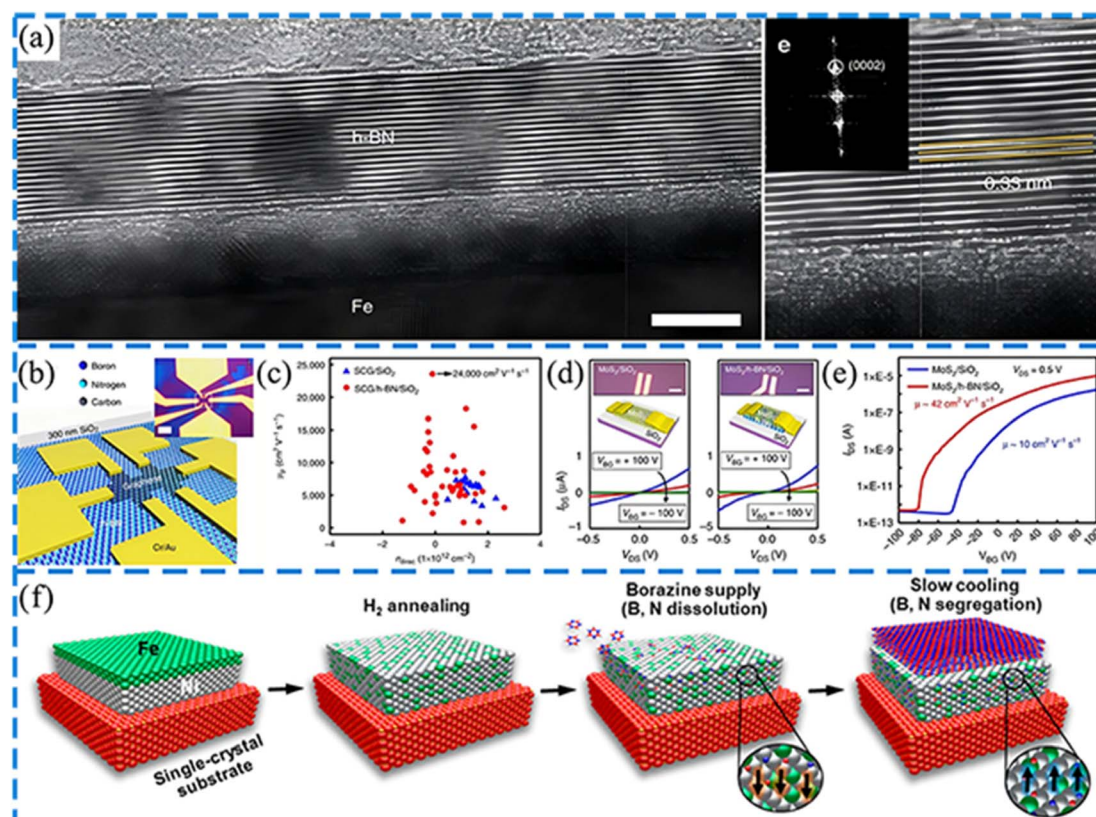

Fig. 11 (a) Cross-sectional TEM images of an as-grown multilayer h-BN film on Fe foil;[101] (b) schematic diagram of the graphene FET on h-BN, scale bar: 10 μm;[101] (c) the plot of the extracted hole mobility (μ_p) versus n_{dirac} for both of the substrates (h-BN and SiO_2);[101] (d) I_{DS}–V_{DS} characteristics of monolayer MoS_2 on SiO_2 (left) and h-BN (right) substrates for various back gate biases between +100 and −100 V with a step of 20 V, scale bar: 10 μm;[101] (e) transfer characteristic curves (I_{DS}–V_{BG}) of the MoS_2 FET on SiO_2 and h-BN substrates at $V_{DS} = 0.5$ V;[101] (f) schematic of the CVD growth of multilayer h-BN on a Ni–Fe alloy film catalyst.[102]

value of ~24 000 cm^2 V^{-1} s^{-1}, which is higher than that for exfoliated h-BN (~13 000 cm^2 V^{-1} s^{-1}).[105] The mobility of the MoS$_2$ FET on the h-BN substrate is four times higher than that on the SiO$_2$ substrate, from 10 cm^2 V^{-1} s^{-1} to 42 cm^2 V^{-1} s^{-1}. In addition, a similar trend has been observed in WSe$_2$ FET devices. However, the device on the h-BN substrate presents an increase in the current level, as shown in Fig. 11(d) and (e).[101]

It was found that higher quality h-BN crystals could be grown by the solution method.[106–110] The crystals grown from molten metal fluxes have fewer defects, less strain and fewer impurities.[111] Li et al. used dissolution and precipitation of N and B on the Fe substrate during heating and cooling to grow high-quality h-BN crystals by the CVD method.[112] Previous studies have shown that the nucleation density of monolayer TMDs (triangular domains per unit area) is directly related to the surface defect density of h-BN substrates.[113,114] Therefore, the defect density of h-BN was subsequently investigated by preparing monolayer WSe$_2$ domains on h-BN flakes by the CVD method. It has a significantly lower nucleation density, averaging 0.56 ± 0.24 μm^{-2}, compared to other monolayer TMD growth using the exfoliated massive h-BN sheets as substrates. A significant reduction in the WSe$_2$ nucleation density implies a low intrinsic point defect density from h-BN flakes. However, using Fe as a catalytic substrate for growing uniform h-BN films faces two issues: (1) the crystal structure of Fe metal changes from body-centered cubic (bcc) to face-centered cubic (fcc) at around 912 °C (while the growth temperature of h-BN is usually 1000–1100 °C), and (2) there is a significant difference in the solubility of B and N atoms in Fe metal, which hinders the uniform segregation of h-BN. Uchida et al. doped Ni and Fe to prepare highly uniform multi-layer h-BN flakes on Ni–Fe alloy thin films; the growth schematic is shown in Fig. 11(f).[102] On the one hand, nickel metal stabilizes the fcc structure, avoiding the transition of the Fe metal lattice structure. On the other hand, the mixture of Ni and Fe metals can regulate the solubility of B and N atoms, achieving a balance of dissolved B and N atoms in the substrate, resulting in uniform segregation of multi-layer h-

BN. The obtained hexagonal boron nitride has a thickness of 2–5 nm and good uniformity.

Chen et al. proposed a new method for synthesizing h-BN under atmospheric pressure.[115] Using gaseous N$_2$ as the precursor, it is easier to control the flow compared to the solid precursors (NH$_3$·BH$_3$ or B$_3$N$_3$H$_6$) previously used. The Ni–B alloy was used as the substrate to directly provide the boron source, reacting with N$_2$ to generate h-BN, breaking the traditional catalytic metal-based growth mechanism and successfully obtaining h-BN on the Ni–B alloy. Compared to previous synthesis methods, this approach allows for the large-scale, high-quality production of h-BN under atmospheric pressure.

3.3 Liquid metal substrates

The distribution and spatial orientation of the h-BN triangular region grown on the solid metal matrix are usually not uniform because the defect locations of the matrix and the grain boundary are more conducive to nucleation. Although the grain boundaries and roughness of the substrate surface can be effectively eliminated and reduced by electrochemical polishing or high temperature annealing, it is still difficult to obtain uniform and neat unidirectional h-BN domains. Khan et al. confirmed the advantages of using molten copper as a catalyst substrate compared with solid copper through a comparative study.[116] The former results in the formation of monocrystalline h-BN, which is a few microns in size and mainly in monolayer and bilayer forms, while the latter produces polycrystalline and mixed multilayers (1−10). The smooth and almost defect-free surface of molten copper is the key to the growth of high-quality h-BN nanosheets, as shown in Fig. 12(e)–(h).

To minimize the adverse effects of grain boundaries on performance and achieve a uniform distribution and consistent spatial orientation of h-BN single crystals, utilized as the gate dielectric layer in highly integrated FETs. Tan et al. used atmospheric pressure chemical vapor deposition (APCVD) technology to fabricate a h-BN self-aligned single-crystals array (SASCA) on
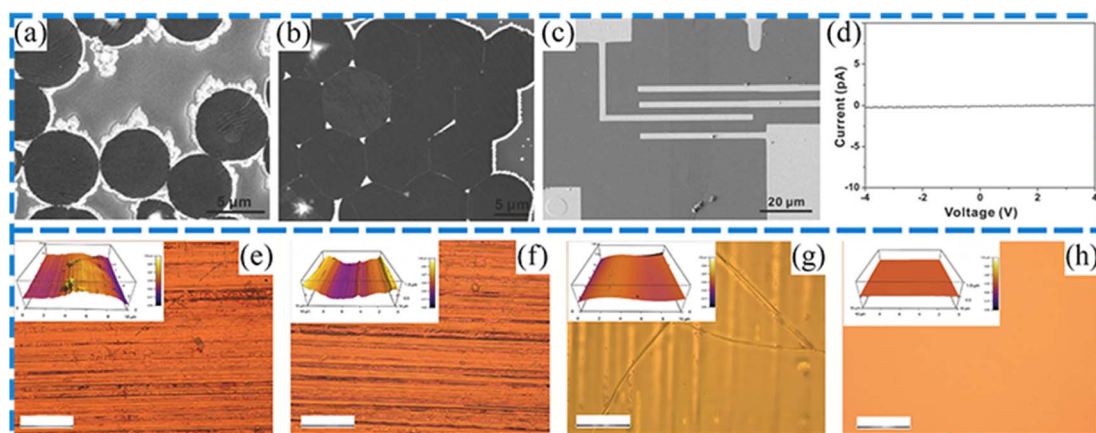

Fig. 12 (a) SEM image of multiple circular h-BN domains;[117] (b) SEM image shows the h-BN SASCA with circular h-BN domains on the edges;[117] (c) SEM image of the h-BN electronic device configuration;[117] (d) the current−voltage curve of h-BN showing excellent electrical insulation properties;[117] (e–h) optical microscope images and Raman spectra of different copper substrates, (e) as-received, (f) 10% HNO$_3$ acid etched, (g) annealed at 1000 °C, and (h) melted at 1100 °C, the scale bar is 50 μm. The inset in each of the images shows the 3D AFM height profile across a 10 × 10 μm^2 area. The color bar is within the 0 to 1 μm range in all the insets.[116]

the liquid Cu surface.[117] This method can obtain isotropic circular domains on the substrate, which can be easily arranged into a tight array with uniform spatial orientation and perfectly self-aligned in the form of hexagons, as shown in Fig. 12(a) and (b). The grown h-BN is a monolayer with a thickness of about 0.73 nm and a very low surface roughness (about 0.19 nm). Then, h-BN electronic devices are prepared to measure the insulation properties of h-BN. It can be seen from the *I–V* curve that no current flows through the device, reflecting its excellent insulation properties, as shown in Fig. 12(c) and (d).

h-BN/transition metal bonding is determined by the hybridization of nitrogen p_z and boron p_z orbitals with metal d_{z^2} states. The strength of this interaction reaches its maximum in the 4d elements Rh and Ru, and decreases to a minimum in the noble metals with the filling of the d shell.[97] Therefore, the lattice mismatch between BN/Au is large and the bonding between the interfaces is very weak.[118] Based on this, Lee *et al.* utilized the CVD method to achieve the fabrication of wafer-scale monolayer two-dimensional h-BN single-crystal films on

a liquid Au substrate through self-collimation grain splicing engineering, as depicted in Fig. 13(a) and (b). After 20 minutes of growth, the grain density increased while the size did not exhibit significant changes (about 14.5 μm). At this point, the electrostatic repulsion between the same type of atoms among different grains caused them to rotate, while the electrostatic attraction between B and N atoms enabled them to form bonds and complete the merging. Through the self-collimated h-BN grains, seamless splicing among different circular grains was realized to form a single-crystal film.[119]

Without special edge-coupled guidance, h-BN domains often grow in the wrong way on statically flat Cu surfaces. The h-BN islands on the solid plane Cu exhibit weak in-plane motion and rotation ability, which limits the general arrangement of h-BN grains after merging. Therefore, rotation and alignment are two key steps to regulate the seamless splicing growth of perfect single crystal h-BN films on atomic planar substrates. Under the control of thermodynamics and dynamics, it has been proved that triangular and circular h-BN domains can be grown on the
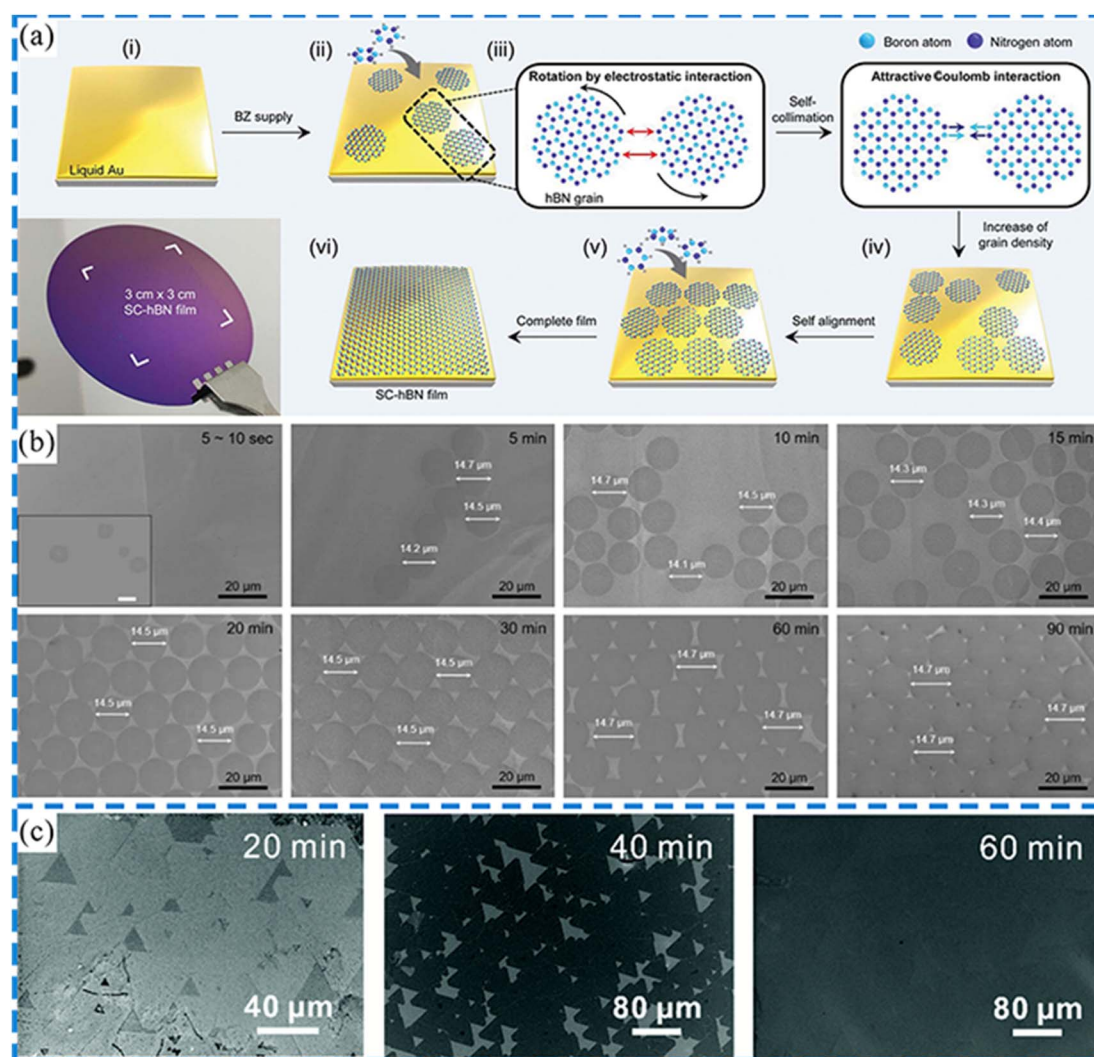

Fig. 13 (a) Schematic illustration of the growth of SC-h-BN films by means of self-collimated circular h-BN grains;[119] (b) effect of growth time on h-BN grain size with constant borazine content observed by SEM;[119] (c) self-aligned epitaxial growth process of h-BN thin films on the liquid Cu surface.[120]

liquid Cu surface, but seamless splicing has not been successfully achieved to obtain a large area of continuous single crystal h-BN films. Zhang *et al.* used double-tube-confined (DTC) atmospheric pressure CVD to realize the facile self-aligned stitching of a quasi-single crystal h-BN monolayer on the surface of liquid Cu.[120] The device uses two sets of concentric quartz tubes of different lengths and diameters to tightly constrain a series of processes such as precursor sublimation, dissociation, vapor transport, adsorption, nucleation, diffusion, maturation, lateral growth, and coalescence within the tubular space. h-BN exhibited discrete antiparallel domains in the initial growth, and with the advance of growth time, the flowing liquid surface would drive the floating h-BN island to rotate and self-collimate, and finally seamlessly splice to obtain continuous quasi-single crystal films, as shown in Fig. 13(c). It is noteworthy that coherent triangular voids exist on the spliced films, proving the uniform seamless splicing of unidirectional domains.

3.4 Sapphire/metal substrates

As previously discussed, single-crystal substrates play an important role in the controlled growth of h-BN using CVD methods. To obtain large-area single-crystal substrates, one can employ methods such as high-temperature annealing or melting and re-solidification of catalytic metal substrates. However, both methods require sustained high temperatures to be maintained for several or even a dozen hours. In the other method, Cu or Ni films are deposited on sapphire (0001) by sputtering or electron-beam deposition, and only about an hour of high-temperature annealing is required to obtain Cu(111) or Ni(111). Single-crystal substrates obtained by this method have been shown to grow wafer-scale single-crystal graphene, and are equally suitable for growing hexagonal boron nitride. This method has demonstrated efficacy in generating single-crystal substrates conducive to the fabrication of wafer-scale single-crystal graphene and is suited for the growth of h-BN.[121]

Uchida *et al.* deposited a ~1 µm thick Cu(111) crystal film on a *c*-plane sapphire substrate using radio frequency (RF) sputtering.[122] Prior to growth, the Cu/sapphire was annealed in a mixture of H_2 and Ar at 1000 °C for 1 hour to enhance the crystallinity and surface smoothness of the Cu film. Subsequently, a monolayer of h-BN was epitaxially grown using an APCVD process, with grain orientation pointing in two main directions. Compared to Cu foil, the Cu film is thin, allowing for easy transfer of the obtained h-BN onto SiO_2/Si substrates using polymethyl methacrylate (PMMA) and ammonium persulfate (APS) water solutions. Researchers also found that the
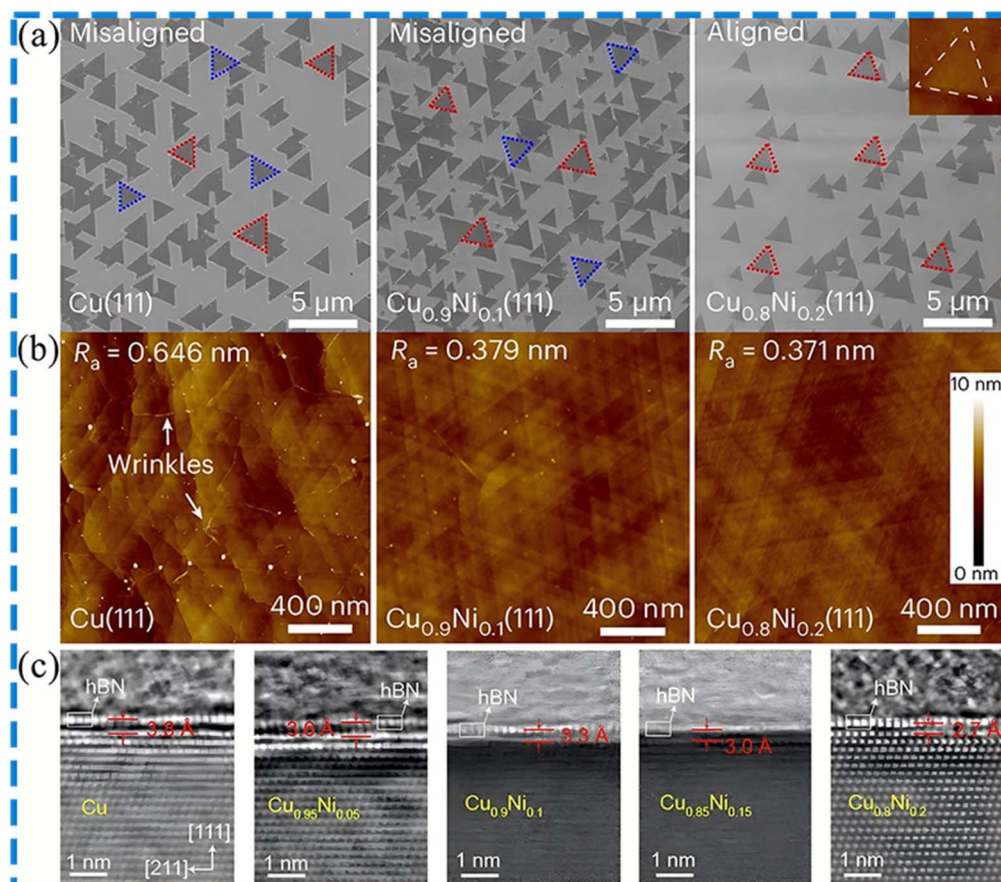
Fig. 14 (a) Scanning electron microscopy (SEM) images of h-BN domains grown on CuNi(111) films with different concentrations of Ni from 0% to 20%. Inset: representative AFM image of an individual h-BN domain; (b) typical AFM images of h-BN films grown on CuNi(111) with different concentrations of Ni from 0% to 20%; (c) cross-section iDPC-STEM images of h-BN grown on Cu(111), $Cu_{0.95}Ni_{0.05}$(111), $Cu_{0.9}Ni_{0.1}$(111), $Cu_{0.85}Ni_{0.15}$(111) and $Cu_{0.8}Ni_{0.2}$(111), respectively.[129]

transferred sapphire can be reused after treatment without affecting the subsequent growth of h-BN. In another study, Alexandre *et al.* sputtered Ni, Cu, and Cu–Ni (Ni 20%) alloy films with a thickness of 500 nm on a *c*-plane sapphire substrate.[123] Under high temperature conditions of 1100 °C, large h-BN grains with lateral sizes exceeding 500 μm were successfully synthesized on the Ni(111) film, with more than 70% of the grains larger than 100 μm. Due to the lower melting temperature of Cu (1084 °C) compared to that of Ni (1455 °C), the Ni(111) film exhibited higher thermal stability than Cu(111) and Cu–Ni(111) alloy films. Even at 1050 °C, severe metal evaporation occurred in Cu and Cu–Ni alloy films. Peter Sutter researched the growth process of preparing h-BN on Ru(0001)/ sapphire by CVD using real-time microscopy and suggested that under sufficiently low precursor pressures (*i.e.*, small B and N supersaturation), the feeble attachment of borazine molecules to the evolving h-BN layer at the growth temperature prompts swift desorption of any adsorbed precursor molecules back into the gaseous phase.[124] Indeed, as the h-BN film grows, it creates an inert layer that progressively extends to fully coat the surfaces of Ru or Pt foil, leading to a gradual decrease in the growth rate of the h-BN layer. Finally, the growth of the film is terminated, forming a thickness of a single atom.

Recently, people have been continuously exploring the growth of high-quality single-crystal h-BN on various metal substrates *via* CVD. However, the fabrication of wafer-scale uniformity of ultra-flat h-BN has not yet been accomplished. Due to the compressive stress relaxation between h-BN and the metallic substrate during high-temperature growth and subsequent cooling, this phenomenon results in the formation of wrinkles and the bunching of underlying metal steps. A rough surface deteriorates h-BN's performance and large-scale uniformity.[125–128] Wang *et al.* fabricated single-crystal CuNi(111)/sapphire wafers through sputtering and annealing processes. By regulating the Ni atom concentration in the substrate, the coupling strength between h-BN and CuNi(111) is adjusted, thereby suppressing the migration of adsorbed atoms and the formation of wrinkles. They ultimately succeeded in preparing ultra-flat single-crystal monolayer h-BN on 4-inch CuNi(111)/sapphire wafers.[129] Through comparison, it is found that the concentration of Ni in the substrate increases from 0 to 20%, and the orientation of the grown h-BN domain and the gap between h-BN and the substrate will change. For example, when the concentration of Ni in the substrate is 10% or 15–20%, the orientation of the h-BN triangle is opposite (0° and 60°) and parallel, respectively. Moreover, as the Ni concentration of CuNi(111) increased, the distance between the grown h-BN and the CuNi(111) substrate gradually decreased. The distance between the h-BN film and $Cu_{0.8}Ni_{0.2}(111)$ was only approximately 2.7 μm, which was significantly smaller than the
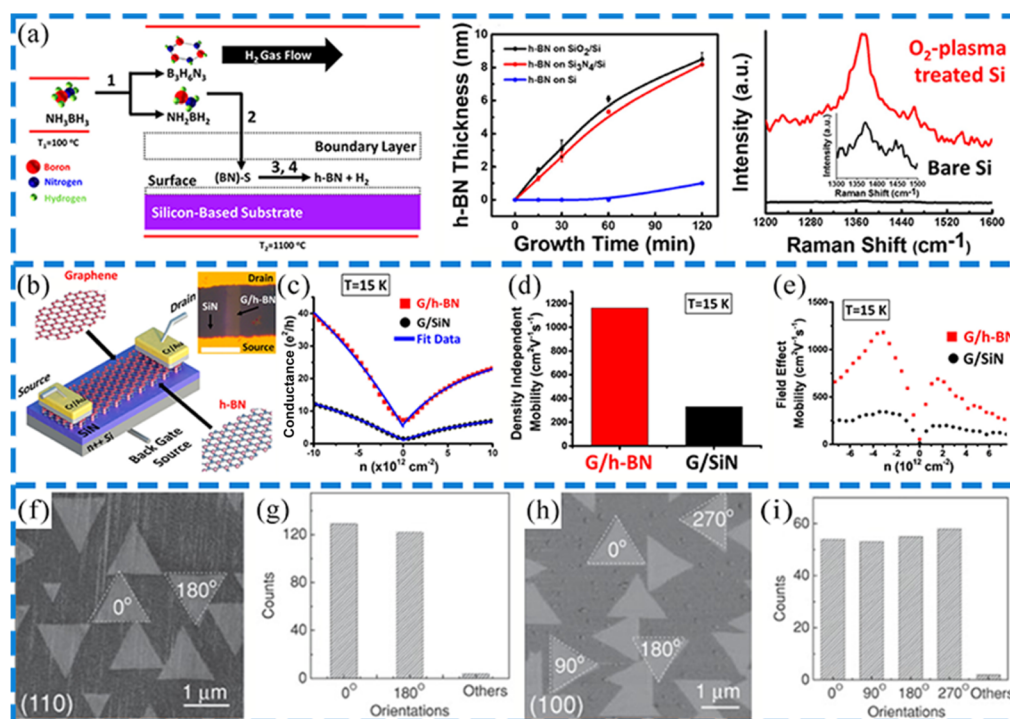

Fig. 15 (a) Schematic of the h-BN growth process (left), the variations of h-BN film thickness at different CVD growth times for Si_3N_4/Si, SiO_2/Si, and Si substrates (middle), Raman spectra of h-BN formations on bare Si and O_2-plasma treated Si, and the inset shows the magnified Raman spectrum of h-BN on bare Si (right);[130] (b) schematic of the G/h-BN heterostructure device with the inset showing the optical microscope image of the back-gated field effect transistor;[130] (c) conductance *vs.* carrier concentration characteristics of G/h-BN and G/SiN heterostructures at 15 K and VDS = 5 mV;[130] (d) the carrier mobility values for both the devices at 15 K;[130] (e) variation of field effect mobility with carrier concentration for G/h-BN and G/SiN heterostructures at 15 K;[130] (f–i) the orientations of h-BN domains grown on Ge(110) and Ge(100); friction force images of h-BN domains grown on (f) Ge(110) and (h) Ge(100), respectively; statistical distribution of the orientations of the h-BN domains grown on (g) Ge(110) and (i) Ge(100), respectively.[131]

Table 1 The summary of CVD-assisted methods under several conditions for the synthesis of mono or few-layer h-BN

Precursor	Substrate	Conditions	Thickness	Lateral size	Domain shape	Ref.
Ammonia borane	Cu foil	(1) Substrate: clean and pickling (dilute nitric acid) (2) Under 425 sccm of Ar and 75 sccm of H₂, Cu foil was annealed at 800 °C for 20 min and then increased up to 1050 °C in 40 min (3) The furnace was heated to 1050 °C for 10–30 min and the precursor was heated to 60 °C. At the same time, the gas flow of Ar and H₂ was reduced to 170 sccm and 30 sccm	1 L	35 μm²	Hexagon	45
Ammonia borane	Cu foil	(1) Substrate: electrochemical polishing followed by annealing (2) After annealing, the H₂ flow rate was reduced to 10 sccm (Ar was stopped) at a pressure of ~10⁻¹ torr (3) The precursor was heated to 70 °C (4) After growth, Cu foil was removed from the hot zone immediately	1–3 L	300 μm	Triangle	53
Borazine	Cu foil	(1) Substrate: clean, electrochemical polishing, followed by annealing (2) The furnace was heated to 1000–1065 °C (3) The precursor was heated to 85 ± 5 °C under 500 sccm of 2.5% H₂/Ar	1 L	20 μm	Triangle, truncated triangle, hexagon	54
Ammonia borane	Cu(111)	(1) Cu foil was electrochemically polished for 30 min (2) The furnace was heated to 1000 °C in 40 min, and the sample was annealed for 2 h in Ar (50 sccm) and H₂ (50 sccm)	1 L	72 μm	Triangle	61
Ammonia borane	Cu(110)	(1) The single crystal Cu(110) substrate was prepared by annealing Cu foil (2) The furnace was heated to 1035 °C under Ar of 500 sccm and H₂ of 50 sccm at atmospheric pressure, then switched to low pressure (about 200 Pa) with Ar (5 sccm) and H₂ (45 sccm) (3) The precursor was heated to 65 °C within 10 min	1 L	Single crystal	Triangle	67
Ammonia borane	Cu(111)	(1) Preparation of Cu(111) on the sapphire substrate (2) The substrate was annealed at 1050 °C for 1 h under a H₂ flow of 300 sccm (3) The precursor was heated to 85 °C and then introduced into the main chamber for 30 min of growth	1 L	Single crystal	Triangle	72
Borazine	Ni foil	(1) Substrate: electrochemical polishing followed by annealing The furnace was heated to 1100 °C at a pressure of 6 mTorr	1–5 L	—	Triangle	77
Borazine	Ni(111)	(1) The single crystal Ni(111) substrate was prepared by annealing Ni foil (2) The precursor flask was placed in an ethanol bath at −15 °C. The bath temperature before the growth was set to 25 °C The furnace was heated to 1220 °C in a flow of Ar (10 sccm) and H₂ (10 sccm). The flow rate of borazine gas was 0.1 sccm	3 L	Single crystal	Truncated triangle	78

Table 1 (*Contd.*)

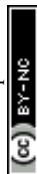| Precursor	Substrate	Conditions	Thickness	Lateral size	Domain shape	Ref.
Borazine	Ir(111)	(1) The substrate was cleaned by Ar$^+$ sputtering and annealed at 1200 °C (2) The furnace was heated to 800–1100 °C under a pressure of 3×10^{-10} mbar	1 L	10 μm	Triangle, trapezoid	86
Diborane, ammonia, hydrogen	Ni foil, Cu foil, sapphire	(1) H$_2$ was introduced at a flow rate of 10 sccm under a pressure of ~10 mTorr (2) The furnace was heated to 800–1000 °C in a flow of precursor (18 sccm) and N$_2$ (5% in H$_2$, 1 sccm)	40–50 nm on Ni, 15 nm on sapphire	—	Triangle	98
Ammonia borane	Cu–Ni alloy	(1) Preparation of the Cu–Ni alloy substrate (2) The furnace was heated to 1050 °C in a H$_2$ flow at a pressure of ~5 kPa (3) For growth, the temperature was changed to 1050–1090 °C under a pressure of 50 Pa (4) The precursor was heated to 70–90 °C	1 L	7500 μm^2	Triangle	87
Ammonia borane	Cu–Si alloy	(1) Preparation of the Cu–Si alloy substrate (2) The pressure was pumped down to 0.1 Pa, H$_2$ flow was supplied and kept a pressure of 50 Pa (3) The substrate was annealed at 1030 °C for 1 h. The precursor was heated to 60–80 °C for 30 min	1 L	0.25 mm	Triangle	88
Borazine	Fe foil	(1) Fe foil was annealed at 1100 °C for 1 h under a 10 sccm H$_2$ flow (2) The furnace was heated to 1100 °C for 30 min. The precursor and H$_2$ were introduced at a rate of 0.1 and 10 sccm, respectively	5–15 nm	—	~2	101
Borazine	Ni–Fe alloy	(1) Preparation of the Ni–Fe alloy substrate by magnetron sputtering (2) The furnace was heated to 1100 °C for 1 h and then introduced the precursor into the CVD chamber at a pressure of ~30 Pa	2–5 nm	—	Triangle	102
Borazine	Au	(1) Au foil and W foil were dipped into Au etchant and Ni etchant for 20 and 10 min to remove impurities (2) The furnace was heated to 1100 °C for 2 h to melt Au foil (3) First step: the precursor was introduced at a flow rate of 0.4 sccm for 50 min under Ar and H$_2$ atmospheres (500 and 40 sccm, respectively) (4) Second step: the flow rate of the precursor was increased to 0.6 sccm for an additional 20 min of growth under other fixed growth conditions	1 L	Single crystal	Circle	119
Borazine	Ru(0001)/ sapphire	(1) Substrate: magnetron sputtering Ru on *c*-axis oriented sapphire (2) h-BN growth was performed in UHV by exposure of the metal surface to the precursor at high temperatures	1 L	—	—	124

Table 1 (Contd.)

Precursor	Substrate	Conditions	Thickness	Lateral size	Domain shape	Ref.
Ammonia borane	$Cu_{0.8}Ni_{0.2}(111)$/sapphire	(1) Preparation of the Cu–Ni alloy substrate on sapphire by magnetron sputtering (2) The furnace was heated to 1000 with 500 sccm Ar and 100 sccm H_2 (3) At 1000 °C the CVD system was switched to 50 torr with 3000 sccm H_2 for 10 min of growth. The precursor was heated to 85 °C	1 L	Single crystal	Triangle	129
Ammonia borane	Si_3N_4/Si, SiO_2/Si	(1) The substrate was cleaned using piranha solution and the furnace was heated to 1100 °C in H_2 (2) The precursor was heated to ~100 °C and transported to the chamber via H_2 carrier gas at a flow rate of 30 sccm (3) The h-BN was prepared at a temperature of 1100 °C under a pressure of 5–10 torr	5–6 nm	—	—	130

approximately 3.8 μm between the h-BN film and Cu(111), as shown in Fig. 14(c). This indicates a strong coupling between h-BN and $Cu_{0.8}Ni_{0.2}(111)$. The strong coupling and high energy difference ensure the mono-orientated growth of h-BN on $Cu_{0.8}Ni_{0.2}(111)$.

The method of depositing melt films on sapphire (0001) by sputtering or electron beam deposition can be effective in saving costs as well as avoiding the long time required for high temperature annealing of single crystal metal foil. However, it is important to note that when utilizing metal/sapphire as a growth substrate for h-BN, precise control of the growth temperature is essential to prevent underlying metal sublimation and brunching.

3.5 Semiconductor substrates

Catalytic metal substrates have unique advantages in the synthesis of two-dimensional materials such as graphene and hexagonal boron nitride. Consequently, a vast amount of effort from scientists has been devoted to this area. However, whether it is the manufacture of 2D heterostructures and devices, an additional wet/dry transfer process is required to transfer them to other desired dielectric substrates. During the transfer process, tears, folds, and wrinkles are inevitably produced, and organic contaminants might also be adsorbed, all of which affect the quality of the film. Therefore, in order to enhance the efficiency and scalability of industrial synthesis of hexagonal boron nitride, it is crucial to obtain large-area hexagonal boron nitride films directly on dielectric substrates without the need for transfer.

Behura et al. achieved large-area, uniform, and smooth growth of h-BN directly on Si-based surfaces through low-pressure chemical vapor deposition, including silicon, silicon nitride (Si_3N_4), and silicon dioxide (SiO_2).[130] They found that as the electronegativity of the substrate increased, Si < Si_3N_4 < SiO_2, the growth rate of h-BN increased, which is consistent with the adsorption rate of precursor molecules calculated by atomic molecular dynamics simulations, as shown in Fig. 15(a). Behura believed that this could be explained by the surface charge of the substrate's top layer. Compared to the planar and neutral surface of Si_3N_4/Si, the presence of negatively charged dangling O atoms in SiO_2/Si results in a faster adsorption rate of borazine molecules. The researchers also discovered that the growth rate of h-BN is higher on O_2 plasma-treated Si surfaces compared to that on bare Si surfaces, further demonstrating the assisting role of oxygen atoms. In addition, polycrystalline graphene/h-BN heterostructure devices were prepared to characterize the properties of h-BN grown by CVD. The device structure is shown in Fig. 15(b). Fig. 15(c) shows that the conductivity is strongly sublinear with respect to the carrier density. This indicates a crossover from low carrier densities (where scattering is mainly caused by charged impurities) to large carrier densities (where short-range impurity scattering predominates).[132] For G/h-BN FET devices, the calculated mobility is 1200 cm^2 V^{-1} s^{-1}. This is about 3.5 times higher than that of G/SiN because coulombic scattering in G/h-BN devices is lower than in G/SiN devices, as shown in Fig. 15(d).[133] It is

known that thicker h-BN films will lead to better isolation of charged impurities, and we can foresee further improvements in carrier mobility and minimum conductivity of G/h-BN devices as the thickness of the h-BN films increases (the h-BN thickness in our devices is 1.5 nm).[134,135] Over the whole range of carrier densities, the mobility of polycrystalline graphene grown directly on the h-BN substrate is enhanced compared to that on the Si_3N_4/Si substrate, as shown in Fig. 15(e). In summary, h-BN grown directly by CVD performs well and contributes to the improvement of mobility in addition to reducing surface roughness and shielding from charged impurities.

Yin *et al.* accomplished large-scale monolayer epitaxial growth of h-BN on the oxide-layer-removed Ge(100) and Ge(110) surfaces *via* the CVD method. Two reversed h-BN triangular h-BN domains were observed on the Ge(110) substrate, while four distinct orientations of triangular domains were witnessed on the Ge(100) substrate, as shown in Fig. 15(g)–(i).[131] The h-BN domains grown on the Ge(110) and Ge(100) surfaces present diverse orientations, mainly attributed to the disparity in crystal plane symmetry between h-BN and Ge. The Ge(110) surface possesses dual symmetry, signifying that the h-BN domain on its surface prefers two opposing orientations, forming h-BN domains with relative orientations. The Ge(100) surface has fourfold symmetry, capable of supporting more orientations, thereby giving rise to two sets of mutually perpendicular and anti-oriented h-BN domains. Earlier studies have suggested that carbon may combine with boron and nitrogen to form a B–C–N layered structure, which provides a new idea for the synthesis of h-BN.[136–140] Sharma *et al.* used the CVD method to prepare h-BN on AlN/sapphire and combined high-resolution TEM and EELS to investigate the effect of carbon on the polycrystalline structure and growth stability of epitaxially grown h-BN films.[141] The findings indicate that after roughly 4 nm of epitaxial growth, h-BN will undergo polycrystalline transformation to r-BN or to disordered t-BN, and even be terminated by a layer of amorphous carbon. Therefore, when using carbon-containing precursors for CVD growth, the concentration of carbon should be controlled to ensure the desired BN structure stability.

4 Conclusion and outlook

h-BN is a two-dimensional ultra-wideband semiconductor material with a graphene-like structure, which is expected to reduce the size of field-effect transistors to the atomic level, and thus revolutionize the current semiconductor industry. In this paper, based on the classification of the epitaxial growth h-BN substrates by the CVD method, the methods and characteristics of epitaxial growth h-BN substrates on solid transition metal substrates, alloy substrates, liquid metal substrates, sapphire/metal substrates and semiconductor substrates are introduced in detail. A comprehensive comparison table of substrates, BN sources, growth conditions and h-BN lateral size has been given, as shown in Table 1.

Solid transition metals are among the most widely used epitaxial substrates for the preparation of h-BN. Due to their unique d-orbital energy level structure, they usually have catalytic activity to promote the nucleation and growth of h-BN. Here is a summary of the traits of typical transition metals used to grow h-BN: the lattice mismatch between Ni(111) and h-BN is only 0.4%, and the structure of both meets 1×1 matching. There is a slight lattice mismatch between Cu(111) and h-BN ($\sim$2%), and the growth rate of h-BN on the Cu(111) plane is faster than that of other orientations. Cu(110) has a step along the $\langle 211 \rangle$ direction, resulting in the C_1 symmetry, which favors the unidirectional arrangement of h-BN domains. There is a superstructure relationship between Pt and h-BN. Solid transition metal as a catalytic substrate also has some defects. For example, substrate materials may be wasted in the process of exfoliating the h-BN film. The h-BN transfer process frequently degrades the film's quality and introduces contaminants. The metal substrate's limited catalytic capability means that it can only be used to prepare a few layers of h-BN, which is not ideal for high-power device applications.[142]

Compared with solid metal substrates, liquid metal substrates offer some novel properties. For example, the ultra-flat surface and self-alignment of h-BN domains on the liquid metal surface. However, in the process of high temperature growth and cooling, compressive stress relaxation will occur, which can easily produce wrinkles and a bunch of underlying metal steps. This increases the h-BN roughness and deteriorates its performance.

At present, semiconductor and sapphire dielectric substrates are both the substrates that need high attention, because device applications usually need to be carried out on a dielectric substrate. Since the sapphire dielectric substrate has no catalytic effect on the growth of h-BN, usually a higher growth temperature is required, and the generated crystal domains are smaller, and the use of lower temperatures to prepare high-quality h-BN is still a problem to be solved.

In conclusion, significant progress has been made in the epitaxy of h-BN on different substrates, but more research is needed on its detailed growth mechanism. Future challenges for h-BN in the chip industry make it necessary to advance the chemical vapor deposition technique in order to produce high-quality, large-area, and commercially feasible h-BN films. In addition, precise doping, modification and regulation of the energy band of h-BN are also valuable areas of research. The 2D layer-by-layer controllable growth of large-area wafer-scale h-BN is less studied, but it is necessary for future applications.

Data availability

Data availability is not applicable to this article as no new data were created or analyzed in this study.

Conflicts of interest

There are no conflicts to declare.

Acknowledgements

References

1 L. Vel, G. Demazeau and J. Etourneau, *Mater. Sci. Eng., B*, 1991, **10**, 149–164.

2 Q. Cai, D. Scullion, W. Gan, A. Falin, S. Zhang, K. Watanabe, T. Taniguchi, Y. Chen, E. Santos and L. H. Li, *Sci. Adv.*, 2019, **5**, v129.

3 K. S. Neo, M. Rahman, X. P. Li, H. H. Khoo, M. Sawa and Y. Maeda, *J. Mater. Process. Technol.*, 2003, **140**, 326–331.

4 A. Falin, Q. Cai, E. Santos, D. Scullion, D. Qian, R. Zhang, Z. Yang, S. Huang, K. Watanabe, T. Taniguchi, M. R. Barnett, Y. Chen, R. S. Ruoff and L. H. Li, *Nat. Commun.*, 2017, **8**, 15815.

5 L. H. Li and Y. Chen, *Adv. Funct. Mater.*, 2016, **26**, 2594–2608.

6 C. Lee, I. Meric, S. Sorgenfrei, K. L. Shepard, C. R. Dean, A. F. Young, L. Wang, J. Hone, P. Kim, T. Taniguchi and K. Watanabe, *Nat. Nanotechnol.*, 2010, **5**, 722–726.

7 S. Moon, J. Kim, J. Park, S. Im, J. Kim, I. Hwang and J. K. Kim, *Adv. Mater.*, 2023, **35**, 2204161.

8 B. P. Singh, *J. Mater. Sci.*, 1987, **22**, 495–498.

9 C. B. Samantaray and R. N. Singh, *Int. Mater. Rev.*, 2005, **50**, 313–344.

10 P. B. Mirkarimi, K. F. Mccarty and D. L. Medlin, *Mater. Sci. Eng., R*, 1997, **21**, 47–100.

11 S. Roy, X. Zhang, A. B. Puthirath, A. Meiyazhagan, S. Bhattacharyya, M. M. Rahman, G. Babu, S. Susarla, S. K. Saju, M. K. Tran, L. M. Sassi, M. A. S. R. Saadi, J. Lai, O. Sahin, S. M. Sajadi, B. Dharmarajan, D. Salpekar, N. Chakingal, A. Baburaj, X. Shuai, A. Adumbumkulath, K. A. Miller, J. M. Gayle, A. Ajnsztajn, T. Prasankumar, V. V. J. Harikrishnan, V. Ojha, H. Kannan, A. Z. Khater, Z. Zhu, S. A. Iyengar, P. A. D. S. Autreto, E. F. Oliveira, G. Gao, A. G. Birdwell, M. R. Neupane, T. G. Ivanov, J. Taha Tijerina, R. M. Yadav, S. Arepalli, R. Vajtai and P. M. Ajayan, *Adv. Mater.*, 2021, **33**, 2101589.

12 S. V. Morozov, K. S. Novoselov, M. I. Katsnelson, F. Schedin, D. C. Elias, J. A. Jaszczak and A. K. Geim, *Phys. Rev. Lett.*, 2008, **100**, 16602.

13 Y. W. Sun, D. G. Papageorgiou, C. J. Humphreys, D. J. Dunstan, P. Puech, J. E. Proctor, C. Bousige, D. Machon and A. San-Miguel, *Appl. Phys. Rev.*, 2021, **8**, 21310.

14 A. A. Balandin, S. Ghosh, W. Bao, I. Calizo, D. Teweldebrhan, F. Miao and C. N. Lau, *Nano Lett.*, 2008, **8**, 902–907.

15 Y. Liu, M. Yang, K. Pang, F. Wang, Z. Xu, W. Gao and C. Gao, *Carbon*, 2020, **156**, 205–211.

16 K. Watanabe, T. Taniguchi and H. Kanda, *Nat. Mater.*, 2004, **3**, 404–409.

17 Y. Kubota, K. Watanabe, O. Tsuda and T. Taniguchi, *Science*, 2007, **317**, 932–934.

18 D. Golberg, Y. Bando, Y. Huang, T. Terao, M. Mitome, C. Tang and C. Zhi, *ACS Nano*, 2010, **4**, 2979–2993.

19 D. Pacilé, J. C. Meyer, Ç. Ö. Girit and A. Zettl, *Appl. Phys. Lett.*, 2008, **92**, 133107.

20 C. Lee, Q. Li, W. Kalb, X. Z. Liu, H. Berger, R. W. Carpick and J. Hone, *Science*, 2010, **328**, 76–80.

21 C. R. Dean, A. F. Young, I. Meric, C. Lee, L. Wang, S. Sorgenfrei, K. Watanabe, T. Taniguchi, P. Kim, K. L. Shepard and J. Hone, *Nat. Nanotechnol.*, 2010, **5**, 722–726.

22 A. Pakdel, Y. Bando and D. Golberg, *Chem. Soc. Rev.*, 2014, **43**, 934–959.

23 Q. Peng, W. Ji and S. De, *Comput. Mater. Sci.*, 2012, **56**, 11.

24 C. Lee, X. Wei, J. W. Kysar and J. Hone, *Science*, 2008, **321**, 385.

25 A. Laturia, M. L. Van de Put and W. G. Vandenberghe, *npj 2D Mater. Appl.*, 2018, **2**, 6.

26 G. Cassabois, P. Valvin and B. Gil, *Nat. Photonics*, 2016, **10**, 262–266.

27 C. Elias, P. Valvin, T. Pelini, A. Summerfield, C. J. Mellor, T. S. Cheng, L. Eaves, C. T. Foxon, P. H. Beton, S. V. Novikov, B. Gil and G. Cassabois, *Nat. Commun.*, 2019, **10**, 2639.

28 G. Cassabois, P. Valvin and B. Gil, *Nat. Photonics*, 2016, **10**, 262.

29 C. Elias, P. Valvin, T. Pelini, A. Summerfield, C. J. Mellor, T. S. Cheng, L. Eaves, C. T. Foxon, P. H. Beton, S. V. Novikov, B. Gil and G. Cassabois, *Nat. Commun.*, 2019, **10**, 2639.

30 H. Liu, J. Meng, X. Zhang, Y. Chen, Z. Yin, D. Wang, Y. Wang, J. You, M. Gao and P. Jin, *Nanoscale*, 2018, **10**, 5559.

31 Y. Kubota, K. Watanabe, O. Tsuda and T. Taniguchi, *Science*, 2007, **317**, 932–934.

32 K. S. Novoselov, A. K. Geim, S. V. Morozov, D. Jiang, Y. Zhang, S. V. Dubonos, I. V. Grigorieva and A. A. Firsov, *Science*, 2004, **306**, 666–669.

33 K. S. Novoselov, D. Jiang, F. Schedin, T. J. Booth, V. V. Khotkevich, S. V. Morozov and A. K. Geim, *Proc. Natl. Acad. Sci. U. S. A.*, 2005, **102**, 10451–10453.

34 W. Han, L. Wu, Y. Zhu, K. Watanabe and T. Taniguchi, *Appl. Phys. Lett.*, 2008, **93**, 223103.

35 J. Ren, L. Stagi, C. M. Carbonaro, L. Malfatti, M. F. Casula, P. C. Ricci, A. E. D. R. Castillo, F. Bonaccorso, L. Calvillo, G. Granozzi and P. Innocenzi, *2D Mater.*, 2020, **7**, 045023.

36 F. Guo, X. Shen, J. Zhou, D. Liu, Q. Zheng, J. Yang, B. Jia, A. K. T. Lau and J.-K. Kim, *Adv. Funct. Mater.*, 2020, **30**, 1910826.

37 Q. Wang, P. Liu, X. Bian, J. Huang, W.-Q. Li, G. Chen and Y. Yang, *Appl. Surf. Sci.*, 2019, **480**, 154–161.

38 K. Y. Ma, L. Zhang, S. Jin, Y. Wang, S. I. Yoon, H. Hwang, J. Oh, D. S. Jeong, M. Wang, S. Chatterjee, G. Kim, A. R. Jang, J. Yang, S. Ryu, H. Y. Jeong, R. S. Ruoff, M. Chhowalla, F. Ding and H. S. Shin, *Nature*, 2022, **606**, 88–93.

39 H. Wang, Y. Zhao, Y. Xie, X. Ma and X. Zhang, *J. Semicond.*, 2017, **38**, 11–24.

40 J. Bao, K. Jeppson, M. Edwards, Y. Fu, L. Ye, X. Lu and J. Liu, *Electron. Mater. Lett.*, 2016, **12**, 1–16.

41 P. R. Kidambi, R. Blume, J. Kling, J. B. Wagner, C. Baehtz, R. S. Weatherup, R. Schloegl, B. C. Bayer and S. Hofmann, *Chem. Mater.*, 2014, **26**, 6380–6392.

42 M. T. Paffett, R. J. Simonson, P. Papin and R. T. Paine, *Surf. Sci.*, 1990, **232**, 286–296.

43 R. Y. Tay, X. Wang, S. H. Tsang, G. C. Loh, R. S. Singh, H. Li, G. Mallick and E. H. Tong Teo, *J. Mater. Chem. C*, 2014, **2**, 1650.

44 M. Corso, W. Auwarter, M. Muntwiler, A. Tamai, T. Greber and J. Osterwalder, *Science*, 2004, **303**, 217.

45 R. Y. Tay, M. H. Griep, G. Mallick, S. H. Tsang, R. S. Singh, T. Tumlin, E. H. Teo and S. P. Karna, *Nano Lett.*, 2014, **14**, 839–846.

46 Y. Shi, C. Hamsen, X. Jia, K. K. Kim, A. Reina, M. Hofmann, A. L. Hsu, K. Zhang, H. Li, Z.-Y. Juang, M. S. Dresselhaus, L.-J. Li and J. Kong, *Nano Lett.*, 2010, **10**, 4134.

47 J. Meng, X. Zhang, Y. Wang, Z. Yin, H. Liu, J. Xia, H. Wang, J. You, P. Jin, D. Wang and X.-M. Meng, *Small*, 2017, **13**, 1604179.

48 M. Morscher, M. Corso, T. Greber and J. Osterwalder, *Surf. Sci.*, 2006, **600**, 3280.

49 M. Corso, T. Greber and J. Osterwalder, *Surf. Sci.*, 2005, **577**, L78.

50 L. Song, L. Ci, H. Lu, P. B. Sorokin, C. Jin, J. Ni, A. G. Kvashnin, D. G. Kvashnin, J. Lou, B. I. Yakobson and P. M. Ajayan, *Nano Lett.*, 2010, **10**, 3209–3215.

51 K. K. Kim, A. Hsu, X. Jia, S. M. Kim, Y. Shi, M. Hofmann, D. Nezich, J. F. Rodriguez-Nieva, M. Dresselhaus, T. Palacios and J. Kong, *Nano Lett.*, 2012, **12**, 161–166.

52 Y. Liu, S. Bhowmick and B. I. Yakobson, *Nano Lett.*, 2011, **11**, 3113–3116.

53 Y. Ji, B. Calderon, Y. Han, P. Cueva, N. R. Jungwirth, H. A. Alsalman, J. Hwang, G. D. Fuchs, D. A. Muller and M. G. Spencer, *ACS Nano*, 2017, **11**, 12057–12066.

54 Y. Stehle, H. M. Meyer, R. R. Unocic, M. Kidder, G. Polizos, P. G. Datskos, R. Jackson, S. N. Smirnov and I. V. Vlassiouk, *Chem. Mater.*, 2015, **27**, 8041–8047.

55 L. Wang, B. Wu, L. Jiang, J. Chen, Y. Li, W. Guo, P. Hu and Y. Liu, *Adv. Mater.*, 2015, **27**, 4858–4864.

56 Y. Liu, S. Bhowmick and B. I. Yakobson, *Nano Lett.*, 2011, **11**, 3113.

57 J. Yin, J. Yu, X. Li, J. Li, J. Zhou, Z. Zhang and W. Guo, *Small*, 2015, **11**, 4497.

58 K. H. Lee, H.-J. Shin, J. Lee, I.-Y. Lee, G.-H. Kim, J.-Y. Choi and S.-W. Kim, *Nano Lett.*, 2012, **12**, 714.

59 M. H. Khan, H. K. Liu, X. Sun, Y. Yamauchi, Y. Bando, D. Golberg and Z. Huang, *Mater. Today*, 2017, **20**, 611.

60 L. Wang, B. Wu, J. Chen, H. Liu, P. Hu and Y. Liu, *Adv. Mater.*, 2014, **26**, 1559–1564.

61 X. Song, J. Gao, Y. Nie, T. Gao, J. Sun, D. Ma, Q. Li, Y. Chen, C. Jin, A. Bachmatiuk, M. H. Rümmeli, F. Ding, Y. Zhang and Z. Liu, *Nano Res.*, 2015, **8**, 3164–3176.

62 J. K. Hite, Z. R. Robinson, C. R. Eddy and B. N. Feigelson, *ACS Appl. Mater. Interfaces*, 2015, **7**, 15200–15205.

63 L. Brown, E. B. Lochocki, J. Avila, C. Kim, Y. Ogawa, R. W. Havener, D. Kim, E. J. Monkman, D. E. Shai, H. I. Wei, M. P. Levendorf, M. Asensio, K. M. Shen and J. Park, *Nano Lett.*, 2014, **14**, 5706–5711.

64 R. Y. Tay, H. J. Park, G. H. Ryu, D. Tan, S. H. Tsang, H. Li, W. Liu, E. H. T. Teo, Z. Lee, Y. Lifshitz and R. S. Ruoff, *Nanoscale*, 2016, **8**, 2434–2444.

65 S. Jin, M. Huang, Y. Kwon, L. Zhang, B. W. Li, S. Oh, J. Dong, D. Luo, M. Biswal, B. V. Cunning, P. V. Bakharev, I. Moon, W. J. Yoo, D. C. Camacho-Mojica, Y. J. Kim, S. H. Lee, B. Wang, W. K. Seong, M. Saxena, F. Ding, H. J. Shin and R. S. Ruoff, *Science*, 2018, **362**, 1021–1025.

66 H. Chen, X. Liu, Y. Huang, G. Li, F. Yu, F. Xiong, M. Zhang, L. Sun, Q. Yang, K. Jia, R. Zou, H. Li, S. Meng, L. Lin, J. Zhang, H. Peng and Z. Liu, *Adv. Mater.*, 2023, **35**, e2209755.

67 L. Wang, X. Xu, L. Zhang, R. Qiao, M. Wu, Z. Wang, S. Zhang, J. Liang, Z. Zhang, Z. Zhang, W. Chen, X. Xie, J. Zong, Y. Shan, Y. Guo, M. Willinger, H. Wu, Q. Li, W. Wang, P. Gao, S. Wu, Y. Zhang, Y. Jiang, D. Yu, E. Wang, X. Bai, Z. J. Wang, F. Ding and K. Liu, *Nature*, 2019, **570**, 91–95.

68 M. Wu, Z. Zhang, X. Xu, Z. Zhang, Y. Duan, J. Dong, R. Qiao, S. You, L. Wang, J. Qi, D. Zou, N. Shang, Y. Yang, H. Li, L. Zhu, J. Sun, H. Yu, P. Gao, X. Bai, Y. Jiang, Z. J. Wang, F. Ding, D. Yu, E. Wang and K. Liu, *Nature*, 2020, **581**, 406–410.

69 X. Xu, Z. Zhang, J. Dong, D. Yi, J. Niu, M. Wu, L. Lin, R. Yin, M. Li, J. Zhou, S. Wang, J. Sun, X. Duan, P. Gao, Y. Jiang, X. Wu, H. Peng, R. S. Ruoff, Z. Liu, D. Yu, E. Wang, F. Ding and K. Liu, *Sci. Bull.*, 2017, **62**, 1074–1080.

70 Y. Hou, B. Wang, L. Zhan, F. Qing, X. Wang, X. Niu and X. Li, *Mater. Today*, 2020, **36**, 10–17.

71 B. Deng, Z. Xin, R. Xue, S. Zhang, X. Xu, J. Gao, J. Tang, Y. Qi, Y. Wang, Y. Zhao, L. Sun, H. Wang, K. Liu, M. H. Rummeli, L.-T. Weng, Z. Luo, L. Tong, X. Zhang, C. Xie, Z. Liu and H. Peng, *Sci. Bull.*, 2019, **64**, 659–668.

72 T. Chen, C. Chuu, C. Tseng, C. Wen, H. S. P. Wong, S. Pan, R. Li, T. Chao, W. Chueh, Y. Zhang, Q. Fu, B. I. Yakobson, W. Chang and L. Li, *Nature*, 2020, **579**, 219–223.

73 L. Wang, X. Xu, L. Zhang, R. Qiao, M. Wu, Z. Wang, S. Zhang, J. Liang, Z. Zhang, Z. Zhang, W. Chen, X. Xie, J. Zong, Y. Shan, Y. Guo, M. Willinger, H. Wu, Q. Li, W. Wang, P. Gao, S. Wu, Y. Zhang, Y. Jiang, D. Yu, E. Wang, X. Bai, Z. J. Wang, F. Ding and K. Liu, *Nature*, 2019, **570**, 91–95.

74 K. V. Bets, N. Gupta and B. I. Yakobson, *Nano Lett.*, 2019, **19**, 2027–2031.

75 M. Muntwiler, W. Auwarter, F. Baumberger, M. Hoesch, T. Greber and J. Osterwalder, *Surf. Sci.*, 2001, **472**, 125–132.

76 H. Oh, J. Jo, Y. Tchoe, H. Yoon, H. H. Lee, S.-S. Kim, M. Kim, B.-K. Sohn and G.-C. Yi, *NPG Asia Mater.*, 2016, **8**, 330.

77 H. Cho, S. Park, D. Won, S. O. Kang, S. Pyo, D. Kim, S. M. Kim, H. C. Kim and M. J. Kim, *Sci. Rep.*, 2015, **5**, 11985.

78 K. Y. Ma, L. Zhang, S. Jin, Y. Wang, S. I. Yoon, H. Hwang, J. Oh, D. S. Jeong, M. Wang, S. Chatterjee, G. Kim, A. R. Jang, J. Yang, S. Ryu, H. Y. Jeong, R. S. Ruoff, M. Chhowalla, F. Ding and H. S. Shin, *Nature*, 2022, **606**, 88–93.

79 L. Vitos, A. V. Ruban, H. L. Skriver and J. Kollar, *Surf. Sci.*, 1998, **411**, 186–202.

80 L. Camilli, E. Sutter and P. Sutter, *2D Materials*, 2014, **1**, 025003.

81 H. Yang, T. Zhang, M. Liu, L. Liu, X. Wu and Y. Wang, *ACS Appl. Electron. Mater.*, 2022, **4**, 891–896.

82 M. T. Paffett, R. J. Simonson, P. Papin and R. T. Paine, *Surf. Sci.*, 1990, **232**, 286–296.

83 G. Kim, A. R. Jang, H. Y. Jeong, Z. Lee, D. J. Kang and H. S. Shin, *Nano Lett.*, 2013, **13**, 1834–1839.

84 K. Suenaga, H. Kobayashi and M. Koshino, *Phys. Rev. Lett.*, 2012, **108**, 075501.

85 Y. Qi, Z. Zhang, B. Deng, X. Zhou, Q. Li, M. Hong, Y. Li, Z. Liu and Y. Zhang, *J. Am. Chem. Soc.*, 2017, **139**, 5849–5856.

86 M. Petrovic, U. Hagemann, M. H. Hoegena and F.-J. M. Heringdorf, *Appl. Surf. Sci.*, 2017, **420**, 504–510.

87 G. Lu, T. Wu, Q. Yuan, H. Wang, H. Wang, F. Ding, X. Xie and M. Jiang, *Nat. Commun.*, 2015, **6**, 6160.

88 J. Li, Z. Hu, Y. Yi, M. Yu, X. Li, J. Zhou, J. Yin, S. Wu and W. Guo, *Small*, 2019, **15**, e1805188.

89 J. R. Reimers, J. Shen, M. Kianinia, C. Bradac, I. Aharonovich, M. J. Ford and P. Piecuch, *Phys. Rev. B*, 2020, **102**, 144105.

90 S. A. Tawfik, S. Ali, M. Fronzi, M. Kianinia, T. T. Tran, C. Stampfl, I. Aharonovich, M. Toth and M. J. Ford, *Nanoscale*, 2017, **9**, 13575–13582.

91 M. Mackoit-Sinkevičienė, M. Maciaszek, C. G. Van de Walle and A. Alkauskas, *Appl. Phys. Lett.*, 2019, **115**, 212101.

92 P. Innocenzi and L. Stagi, *Acc. Mater. Res.*, 2024, **5**, 413–425.

93 A. B. Preobrajenski, A. S. Vinogradov and N. Martensson, *Surf. Sci.*, 2005, **582**, 21–30.

94 A. B. Preobrajenski, A. S. Vinogradov, M. L. Ng, E. Cavar, R. Westerstrom, A. Mikkelsen, E. Lundgren and N. Martensson, *Phys. Rev. B:Condens. Matter Mater. Phys.*, 2007, **75**, 245412.

95 R. Laskowski and P. Blaha, *Phys. Rev. B:Condens. Matter Mater. Phys.*, 2010, **81**, 075418.

96 A. B. Preobrajenski, M. A. Nesterov, M. L. Ng, A. S. Vinogradov and N. Martensson, *Chem. Phys. Lett.*, 2007, **446**, 119.

97 R. Laskowski, P. Blaha and K. Schwarz, *Phys. Rev. B:Condens. Matter Mater. Phys.*, 2008, **78**, 045409.

98 A. Ismach, H. Chou, D. A. Ferrer, Y. Wu, S. Mcdonnell, H. C. Floresca, A. Covacevich, C. Pope, R. Piner, M. J. Kim, R. M. Wallace, L. Colombo and R. S. Ruoff, *ACS Nano*, 2012, **6**, 6378–6385.

99 G. Lu, T. Wu, P. Yang, Y. Yang, Z. Jin, W. Chen, S. Jia, H. Wang, G. Zhang, J. Sun, P. M. Ajayan, J. Lou, X. Xie and M. Jiang, *Adv. Sci.*, 2017, **4**, 1700076.

100 S. M. Kim, A. Hsu, M. H. Park, S. H. Chae, S. J. Yun, J. S. Lee, D. Cho, W. Fang, C. Lee, T. Palacios, M. Dresselhaus, K. K. Kim, Y. H. Lee and J. Kong, *Nat. Commun.*, 2015, **6**, 8662.

101 S. M. Kim, A. Hsu, M. H. Park, S. H. Chae, S. J. Yun, J. S. Lee, D.-H. Cho, W. Fang, C. Lee, T. Palacios, M. Dresselhaus, K. K. Kim, Y. H. Lee and J. Kong, *Nat. Commun.*, 2015, **6**, 8662.

102 Y. Uchida, S. Nakandakari, K. Kawahara, S. Yamasaki, M. Mitsuhara and H. Ago, *ACS Nano*, 2018, **12**, 6236–6244.

103 C. R. Dean, A. F. Young, I. Meric, C. Lee, L. Wang, S. Sorgenfrei, K. Watanabe, T. Taniguchi, P. Kim, K. L. Shepard and J. Hone, *Nat. Nanotechnol.*, 2010, **5**, 722–726.

104 L. M. Malard, M. A. Pimenta, G. Dresselhaus and M. S. Dresselhaus, *Phys. Rep.*, 2009, **473**, 51–87.

105 W. Gannett, W. Regan, K. Watanabe, T. Taniguchi, M. F. Crommie and A. Zettl, *Appl. Phys. Lett.*, 2011, **98**, 242105.

106 M. Y. K. Yap, M. O. M. Okamoto, M. O. M. Onda, M. Y. M. Yoshimura, Y. M. Y. Mori and T. S. T. Sasaki, *Jpn. J. Appl. Phys.*, 2000, **39**, L300.

107 N. D. Zhigadlo, *J. Cryst. Growth*, 2014, **402**, 308–311.

108 T. Taniguchi and K. Watanabe, *J. Cryst. Growth*, 2007, **303**, 525–529.

109 Y. Kubota, K. Watanabe and T. Taniguchi, *Jpn. J. Appl. Phys.*, 2007, **46**, 311.

110 T. B. Hoffman, B. Clubine, Y. Zhang, K. Snow and J. H. Edgar, *J. Cryst. Growth*, 2014, **393**, 114–118.

111 Z. Fisk and J. P. Remeika, *Handbook on the Physics and Chemistry of Rare Earths*, 1989, vol. 12, pp. 53–70.

112 J. Li, J. Wang, X. Zhang, C. Elias, G. Ye, D. Evans, G. Eda, J. M. Redwing, G. Cassabois, B. Gil, P. Valvin, R. He, B. Liu and J. H. Edgar, *ACS Nano*, 2021, **15**, 7032–7039.

113 X. Zhang, F. Zhang, Y. Wang, D. S. Schulman, T. Zhang, A. Bansal, N. Alem, S. Das, V. H. Crespi, M. Terrones and J. M. Redwing, *ACS Nano*, 2019, **13**, 3341–3352.

114 F. Zhang, Y. Wang, C. Erb, K. Wang, P. Moradifar, V. H. Crespi and N. Alem, *Phys. Rev. B*, 2019, **99**, 155430.

115 D. Chen, H. Shen, B. Liu, Z. Wang, B. Liao, W. Mao, Y. Li and T. Wu, *J. Electron. Mater.*, 2023, **52**, 4913–4920.

116 M. H. Khan, Z. Huang, F. Xiao, G. Casillas, Z. Chen, P. J. Molino and H. K. Liu, *Sci. Rep.*, 2015, **5**, 7743.

117 L. Tan, J. Han, R. G. Mendes, M. H. Rümmeli, J. Liu, Q. Wu, X. Leng, T. Zhang, M. Zeng and L. Fu, *Adv. Electron. Mater.*, 2015, **1**, 1500223.

118 L.-P. Ding, Y. J. Guo, J. H. Zeng, Z. A. Guo, Y.-R. Zhao and P. Shao, *J. Phys. Chem. C*, 2024, **128**, 234–241.

119 J. S. Lee, S. H. Choi, S. J. Yun, Y. I. Kim, S. Boandoh, J. H. Park, B. G. Shin, H. Ko, S. H. Lee, Y. M. Kim, Y. H. Lee, K. K. Kim and S. M. Kim, *Science*, 2018, **362**, 817–821.

120 Q. Zhang, H. Chen, S. Liu, Y. Yu, C. Wang, J. Han, G. Shao and Z. Yao, *Nanoscale*, 2022, **14**, 3112–3122.

121 K. Verguts, B. Vermeulen, N. Vrancken, K. Schouteden, C. Van Haesendonck, C. Huyghebaert, M. Heyns, S. De Gendt and S. Brems, *J. Phys. Chem. C*, 2016, **120**, 297–304.

122 Y. Uchida, T. Iwaizako, S. Mizuno, M. Tsuji and H. Ago, *Phys. Chem. Chem. Phys.*, 2017, **19**, 8230–8235.

123 A. B. Taslim, H. Nakajima, Y. Lin, Y. Uchida, K. Kawahara, T. Okazaki, K. Suenaga, H. Hibino and H. Ago, *Nanoscale*, 2019, **11**, 14668–14675.

124 P. Sutter, J. Lahiri, P. Albrecht and E. Sutter, *ACS Nano*, 2011, **5**, 7303–7309.

125 B. Deng, J. Wu, S. Zhang, Y. Qi, L. Zheng, H. Yang, J. Tang, L. Tong, J. Zhang, Z. Liu and H. Peng, *Small*, 2018, **14**, 1800725.

126 L. Zheng, N. Liu, X. Gao, W. Zhu, K. Liu, C. Wu, R. Yan, J. Zhang, X. Gao, Y. Yao, B. Deng, J. Xu, Y. Lu, Z. Liu, M. Li, X. Wei, H. W. Wang and H. Peng, *Nat. Methods*, 2023, **20**, 123–130.

127 B. Deng, Z. Pang, S. Chen, X. Li, C. Meng, J. Li, M. Liu, J. Wu, Y. Qi, W. Dang, H. Yang, Y. Zhang, J. Zhang, N. Kang, H. Xu, Q. Fu, X. Qiu, P. Gao, Y. Wei, Z. Liu and H. Peng, *ACS Nano*, 2017, **11**, 12337–12345.

128 G. Yuan, D. Lin, Y. Wang, X. Huang, W. Chen, X. Xie, J. Zong, Q.-Q. Yuan, H. Zheng, D. Wang, J. Xu, S.-C. Li, Y. Zhang, J. Sun, X. Xi and L. Gao, *Nature*, 2020, **577**, 204–208.

129 Y. Wang, C. Zhao, X. Gao, L. Zheng, J. Qian, J. Gao, J. Li, J. Tang, C. Tan, J. Wang, X. Zhu, J. Guo, Z. Liu, F. Ding and H. Peng, *Nat. Mater.*, 2024, **23**, 1495–1501.

130 S. Behura, P. Nguyen, R. Debbarma, S. Che, M. R. Seacrist and V. Berry, *ACS Nano*, 2017, **11**, 4985–4994.

131 J. Yin, X. Liu, W. Lu, J. Li, Y. Cao, Y. Li, Y. Xu, X. Li, J. Zhou, C. Jin and W. Guo, *Small*, 2015, **11**, 5375–5380.

132 K. Nomura and A. H. MacDonald, *Phys. Rev. Lett.*, 2007, **98**, 076602.

133 S. Adam, E. H. Hwang, V. M. Galitski and S. Das Sarma, *Proc. Natl. Acad. Sci. U. S. A.*, 2007, **104**, 18392–18397.

134 J. M. Xue, J. Sanchez-Yamagishi, D. Bulmash, P. Jacquod, A. Deshpande, K. Watanabe, T. Taniguchi, P. Jarillo-Herrero and B. J. Leroy, *Nat. Mater.*, 2011, **10**, 282–285.

135 D. Wong, J. Velasco, L. Ju, J. Lee, S. Kahn, H.-Z. Tsai, C. Germany, T. Taniguchi, K. Watanabe, A. Zettl, F. Wang and M. F. Crommie, *Nat. Nanotechnol.*, 2015, **10**, 949–953.

136 L. Ci, L. Song, C. Jin, D. Jariwala, D. Wu, Y. Li, A. Srivastava, Z. F. Wang, K. Storr, L. Balicas, F. Liu and P. M. Ajayan, *Nat. Mater.*, 2010, **9**, 430.

137 Z. Liu, L. Song, S. Zhao, J. Huang, L. Ma, J. Zhang, J. Lou and P. M. Ajayan, *Nano Lett.*, 2011, **11**, 2032.

138 L. Song, Z. Liu, A. L. M. Reddy, N. T. Narayanan, J. Taha-Tijerina, J. Peng, C. Gao, J. Lou, R. Vajtai and P. M. Ajayan, *Adv. Mater.*, 2012, **24**, 4878.

139 Z. Liu, L. Ma, C. Shi, W. zhou, Y. Gong, S. Lei, X. Yang, J. zhang, J. Yu, K. P. Hackenberg, A. Babakhani, J.-C. Idrobo, R. Vajtai, J. Lou and P. M. Ajayan, *Nat. Nanotechnol.*, 2013, **8**, 119.

140 B. Muchharla, A. Pathak, Z. Liu, L. Song, T. Jayasekera, S. Kar, R. Vajtai, L. Balicas, P. M. Ajayan, S. Talapatra and N. Ali, *Nano Lett.*, 2013, **13**, 3476.

141 S. Sharma, J. Palisaitis, I. G. Ivanov, P. O. Persson, H. Pedersen and H. Högberg, *Adv. Mater. Interfaces*, 2024, **11**, 2400091.

142 G. Wang and X. Zhang, *J. Synth. Cryst.*, 2023, **52**, 825.